Author Manuscript

Author Manuscript

Author Manuscript

Author Manuscript

HHS Public Access

Author manuscript

Cell Rep. Author manuscript; available in PMC 2022 February 28.

Published in final edited form as:

Cell Rep. 2022 February 08; 38(6): 110353. doi:10.1016/j.celrep.2022.110353.

A comprehensive landscape of 60S ribosome biogenesis factors

Carolin Sailer[1,2,4], **Jasmin Jansen**[1,2,4], **Kamil Sekulski**[3], **Victor E. Cruz**[3], **Jan P. Erzberger**[3,*], **Florian Stengel**[1,2,5,*]

[1]Department of Biology, University of Konstanz, Universitätsstrae 10, 78457 Konstanz, Germany

[2]Konstanz Research School Chemical Biology, University of Konstanz, Universitätsstrae 10, 78457 Konstanz, Germany

[3]Department of Biophysics, UT Southwestern Medical Center - ND10.124B, 5323 Harry Hines Boulevard, Dallas, TX 75390-8816, USA

[4]These authors contributed equally

[5]Lead contact

SUMMARY

Eukaryotic ribosome biogenesis is facilitated and regulated by numerous ribosome biogenesis factors (RBFs). High-resolution cryoelectron microscopy (cryo-EM) maps have defined the molecular interactions of RBFs during maturation, but many transient and dynamic interactions, particularly during early assembly, remain uncharacterized. Using quantitative proteomics and crosslinking coupled to mass spectrometry (XL-MS) data from an extensive set of pre-ribosomal particles, we derive a comprehensive and time-resolved interaction map of RBF engagement during 60S maturation. We localize 22 previously unmapped RBFs to specific biogenesis intermediates and validate our results by mapping the catalytic activity of the methyltransferases Bmt2 and Rcm1 to their predicted nucleolar 60S intermediates. Our analysis reveals the interaction sites for the RBFs Noc2 and Ecm1 and elucidates the interaction map and timing of 60S engagement by the DEAD-box ATPases Dbp9 and Dbp10. Our data provide a powerful resource for future studies of 60S ribosome biogenesis.

Graphical Abstract

This is an open access article under the CC BY-NC-ND license (http://creativecommons.org/licenses/by-nc-nd/4.0/).

*Correspondence: jan.erzberger@utsouthwestern.edu (J.P.E.), florian.stengel@uni-konstanz.de (F.S.).

AUTHOR CONTRIBUTIONS

C.S., J.J., J.P.E., and F.S. conceived the study and experimental approach. C.S. expressed, purified, and crosslinked pre-ribosomal particles, with help from J.J. C.S. implemented and applied the mi-filter. J.J., K.S., and V.E.C. validated the timeline. C.S., J.J., J.P.E. and F.S. analyzed the data. C.S., J.P.E., and F.S. wrote the paper, with input from all of the authors.

SUPPLEMENTAL INFORMATION

Supplemental information can be found online at https://doi.org/10.1016/j.celrep.2022.110353.

DECLARATION OF INTERESTS

The authors declare no competing interests.

Author Manuscript Author Manuscript Author Manuscript Author Manuscript

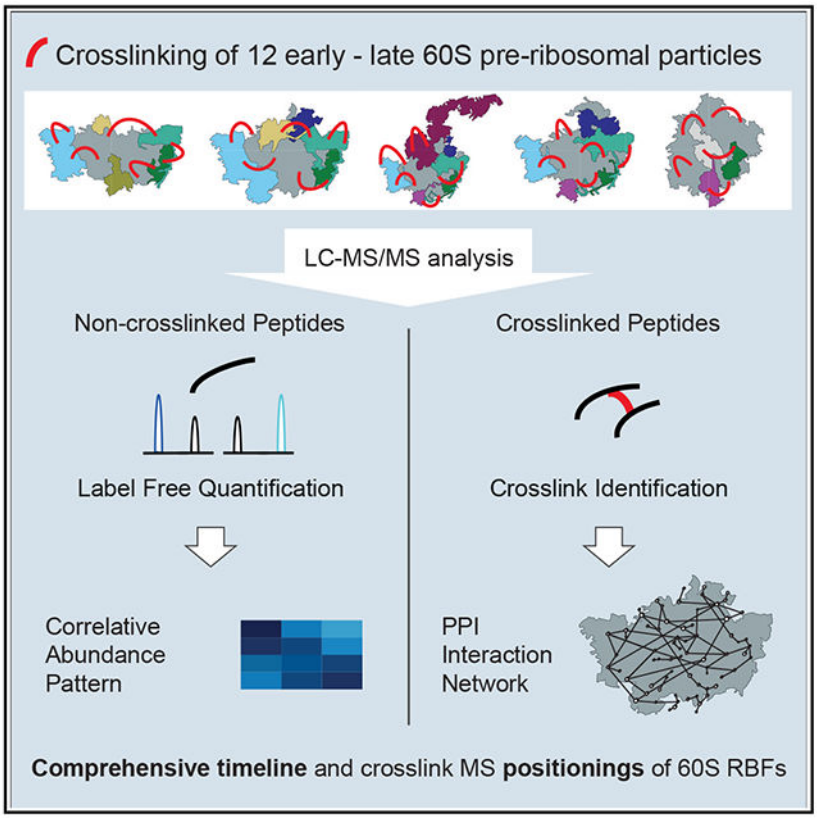

In brief

In this study, Sailer et al. generate a comprehensive and precise timeline of ribosome biogenesis factor (RBF) engagement during 60S maturation and localize previously unmapped RBFs in the yeast *Saccharomyces cerevisiae*. Overall, their data represent an essential resource for future structural studies of large subunit ribosome biogenesis.

INTRODUCTION

Ribosome biogenesis is a complex, multistep maturation process that assembles protein and RNA components across multiple cellular compartments to generate mature ribosomes. Approximately 200 ribosomal biogenesis factors (RBFs) engage pre-ribosomes during assembly but are not components of mature ribosomes (Woolford and Baserga, 2013; Konikkat and Woolford, 2017; Klinge and Woolford, 2019; Kressler et al., 2017). RBFs are crucial for the precise processing of 35S rRNA into mature rRNAs and for the ordered incorporation of ribosomal proteins (r-proteins) during biogenesis. RBFs achieve this by engaging specific intermediate states and by guiding structural and conformational rearrangements of the rRNA during maturation. Changes in RBF composition correlate with the movement of pre-ribosomes from the nucleolus to the cytoplasm, suggesting that RBF composition guides the cellular movement of pre-ribosomes. Depending on their individual functions, some RBFs engage maturing ribosomes transiently, while others remain bound for prolonged periods during biogenesis.

Author Manuscript Author Manuscript Author Manuscript Author Manuscript

The focus of this study is the 60S biogenesis pathway in the yeast *Saccharomyces cerevisiae*, beginning with intermediates that immediately precede the physical separation of 18S and 27S rRNA after 35S cleavage at the A2 site within the internal transcribed spacer 1 (ITS1). Initially, studies of 60S biogenesis focused on rRNA processing events, especially the precise, multi-step excision of ITS2 and on the proteomic characterizations of various affinity-purified biogenesis intermediates (Gamalinda et al., 2014; Woolford and Baserga, 2013). While these studies have provided a broad catalog and a coarse timeline of the biogenesis factors involved in pre-60S maturation, a rigorous quantitative analysis of the entire pre-60S assembly proteome has not been carried out to date. More recently, multiple cryoelectron microscopy (cryo-EM) reconstructions of 60S pre-ribosomal particles have allowed the structural mapping of many assembly factors (AFs) (Kargas et al., 2019; Kater et al., 2017, 2020; Sanghai et al., 2018; Wu et al., 2016; Zhou et al., 2019a, 2019b).

Despite this remarkable assortment of structural models, the low abundance and inherent dynamics of pre-60S assemblies still make it extremely challenging to resolve structures of more transient assembly intermediates or to visualize dynamic regions, something that is particularly true for early nucleolar assembly intermediates. This is reflected in the fact that no structural or functional information exists for over half of the known RBFs associated with 60S biogenesis.

Among ribosome biogenesis factors whose structural role has remained elusive are seven members of the DEAD-box family of ATPases. These proteins are thought to play fundamental roles in ribosome biogenesis, catalyzing energy-consuming RNA remodeling events to unidirectionally drive specific maturation steps during ribosome assembly (Klinge and Woolford, 2019; Martin et al., 2013; Rodríguez-Galán et al., 2013). To date, of the 8 DEAD-box ATPases associated with 60S biogenesis, only Has1 has been successfully positioned in high-resolution cryo-EM maps of 60S pre-ribosomal particles (Kater et al., 2017; Sanghai et al., 2018; Zhou et al., 2019a).

In this study, we used large-scale biochemical enrichments of a comprehensive set of 60S pre-ribosomal particles in the yeast *S. cerevisiae* to identify and quantify individual RBF abundances within 60S intermediates. A clustering analysis of the nearly 20,000 individual datapoints in this dataset resulted in a comprehensive and precise timeline of RBF engagement during 60S maturation. Furthermore, crosslinking coupled to mass spectrometry (XL-MS) was used to expand our current knowledge of direct interaction partners for individual RBFs. Combined, these data allow us to expand the 60S engagement profile of structurally characterized factors, to localize structurally uncharacterized RBFs, and to identify additional proteins with a potential role in 60S biogenesis. Overall, our comprehensive data represent an essential resource for future structural studies of large subunit ribosome biogenesis.

RESULTS

An overall timeline of 60S biogenesis derived from quantitative MS data

To generate a comprehensive, time-resolved dataset of RBF engagement during 60S biogenesis, we selected RBFs covering the entire 60S maturation pathway as baits for the

Author Manuscript Author Manuscript Author Manuscript Author Manuscript

large-scale biochemical enrichment of 60S pre-ribosomal particles. Samples were analyzed using our integrated affinity-purification label-free quantification and XL-MS (AP-MS LFQ/XL-MS) workflow (Figure 1A). This strategy allowed us to simultaneously generate a precise proteomic profile of RBF abundance by identifying and quantifying non-crosslinked peptides in each sample, thereby reconstructing the overall timeline of 60S ribosomal biogenesis, and to define the protein interaction network for each of the purified pre-ribosomal particles using chemical crosslinking (Figure 1A). In total, the affinity purification of 36 independently purified samples from 12 different RBFs allowed us to reliably quantify 272 proteins using MaxQuant (Tyanova et al., 2016a; Hein et al., 2015) in combination with the Perseus package for statistical validation (Tyanova et al., 2016b) (Figures 1B-1D and S1-S4, Table S1; see STAR Methods for details).

Unbiased hierarchical clustering based on similarities in measured protein abundances shows that biological replicates always cluster together, reflecting the robustness and reproducibility of our sample purification and analysis workflow (Figure S1). The clustering analysis places 60S intermediates purified with affinity-tagged Noc1 at the beginning of the timeline, followed by intermediates containing Rsa3, Ssf1, Nop16, Ytm1, Nsa1, Cic1, Rix1, Nop12, Nog2, Arx1, and Lsg1 (Figure S1). This timeline is broadly consistent with previous structural, biochemical, and genetic studies (Woolford and Baserga, 2013; Klinge and Woolford, 2019; Kressler et al., 2010, 2017). Nine of our baits (Ssf1, Nop16, Ytm1, Nsa1, Cic1, Rix1, Nog2, Arx1, and Lsg1) have been identified and modeled in cryo-EM reconstructions (Kargas et al., 2019; Kater et al., 2017, 2020; Sanghai et al., 2018; Wu et al., 2016; Zhou et al., 2019a, 2019b), and their distribution among known 60S intermediate structures is consistent with the timeline derived from our MS data (Figure 2A). Our other bait RBFs (Noc1, Rsa3, and Nop12) have not been identified in any 60S structural reconstructions to date. In line with previous proteomic studies (de la Cruz et al., 2004; Milkereit et al., 2001), our analysis places Noc1 and Rsa3 at the early end of our timeline, with a protein distribution pattern that is distinct from later intermediates (Figure 1B). In particular, the presence of the RBFs Rrp5, Rok1, and Rex4, critical mediators of ITS1 processing (Eppens et al., 2002; Khoshnevis et al., 2016), other RBFs associated with small subunit biogenesis, and 40S r-proteins, suggests that these intermediates span the cleavage of 35S into small and large ribosomal rRNA fragments, and thus represent the earliest independent pre-60S complexes. Intermediates purified using affinity-tagged Nop12 cluster with nucleoplasmic intermediates containing Nog2 and Rix1 in our overall timeline of 60S ribosome biogenesis. However, the pattern of particles purified with affinity-tagged Nop12 shows additional complexity and some enrichment with proteins linked to early or early to intermediate nucleolar 60S assembly stages (Figures 1B-1D, S2, and S3), thus not ruling out a broader involvement of Nop12 in 60S biogenesis.

Our final dataset contains a total of 131 proteins previously annotated as ribosome biogenesis factors in the literature (Woolford and Baserga, 2013) or in the *Saccharomyces* genome database (SGD) (Cherry et al., 2012). Of these 131 RBFs, 77 have been modeled at atomic resolution into cryo-EM maps of pre-40S (28 RBFs) and pre-60S (49 RBFs) ribosomal intermediates (Barandun et al., 2017; Cheng et al., 2017; Kargas et al., 2019; Kater et al., 2017, 2020; Kornprobst et al., 2016; Schuller et al., 2018; Wu et al., 2016; Zhou et al., 2019a). The presence of pre-40S RBFs in the early stages of our timeline

Author Manuscript Author Manuscript Author Manuscript Author Manuscript

indicates that some of our earliest pre-60S samples are still tethered to pre-40S particles via ITS1 and that our samples therefore encompass the entire 60S assembly landscape. In total, we reliably identify and quantify 49 of the 53 RBFs modeled into cryo-EM maps of 60S pre-ribosomal particles (the missing factors are Cgr1, Ria1, Sdo1, and Rtc3) (Figures 1C and S3; Table S1: “Quantified RBFs with known positions in pre-60S cryo-EM structures” and “Quantified RBFs with known positions in 90S, pre-40S, and pre-60S cryo-EM structures”). The near-complete coverage of previously localized 60S RBFs and the accurate clustering of characterized RBFs validate our approach and speak to the high reliability of our dataset. In addition to the 49 RBFs with established positions in pre-60S particles, we identify and quantify an additional 47 (of the remaining 54) proteins in our dataset that have been linked to large subunit biogenesis through biochemical and genetic studies (Woolford and Baserga, 2013; Cherry et al., 2012) (Figure 1D; Table S1: “Quantified unmapped RBFs”).

The peptides of an additional 82 non-ribosomal proteins can be readily detected and quantified in our samples (Figure S4; Table S1: “Quantified additional proteins”). The known functions, high cellular abundance and lack of an obvious link to ribosome biogenesis suggest that most of these proteins are minor contaminants in our purifications. However, a subset of factors may play a role in 60S assembly, although their exclusion from previous proteomics studies suggests that they may have a more peripheral or regulatory role in biogenesis. Of these, the most intriguing candidates are Tma16, Nap1, Lhp1, Pab1, Sro9, YMR310C, YGR283C, and YCR016W. Tma16 was identified in a screen for ribosome-associated factors (Fleischer et al., 2006) and recently identified in a human ribosomal intermediate (Liang et al., 2020). We confirmed the presence of a similar Tma16-containing particle in yeast (Figure S4). Nap1, among other functions, chaperones Rps6 and may directly facilitate 40S biogenesis (Rössler et al., 2019); Lhp1 is a yeast La protein homolog required for the maturation of tRNAs and could plausibly have a function in ribosome biogenesis (Yoo and Wolin, 1997). Pab1 is traditionally associated with mRNA processing, but it also has genetic interactions with ribosome biogenesis factors Spb1 and Spb4 and with eL43 (Sachs and Davis, 1990); Sro9 is an RNA-binding protein that associates with translating ribosome but also shuttles between the nucleus and cytoplasm (Röther et al., 2010); YMR310C and YGR283C are uncharacterized paralogs with predicted methyltransferase function, which were recently annotated as being associated with the RBFs Urb1 and Urb2. These open reading frames (ORFs), along with the gene encoding another nucleolar protein present in our dataset, YCR016W, are part of a large ribosome biogenesis regulon (Wade et al., 2006).

Assignment of unmapped factors to distinct 60S intermediate structures and validation of our proposed timeline

Pre-60S structural intermediates can be broadly divided into nucleolar, nucleoplasmic, and cytoplasmic assemblies, characterized by distinct rRNA processing states and compartment-specific RBFs. Characteristic differences in RBF composition can therefore be used to associate structurally uncharacterized RBFs with individual pre-60S cryo-EM structures. For our analysis, we chose two representative structures for each subcellular compartment (Figure 2A). As our quantitative data mirror the changes in RBF composition of these structures, we can use individual abundance correlations between these “marker” RBFs and

Author Manuscript Author Manuscript Author Manuscript Author Manuscript

unmapped RBFs to assign them to specific structural intermediates. In addition, we can expand the presence of structurally characterized factors to intermediates, where they are associated with dynamic regions that are not currently resolvable in cryo-EM maps (Figure 2A). The correlation between early and late nucleolar RBFs and components of the 5S rRNP (uL5, uL18, Rrs1, and Rpf2) (Figures 1C and S2) indicates that the 5S rRNP is recruited to the maturing 60S particle at an early stage, before it is resolvable in cryo-EM maps, possibly after the release of Mak11 and the binding of Nog1, Mrt4, Nsa2, and uL6. This is consistent with the presence of 5S in northern blots of ribosomal intermediates purified with affinity tags on Ssf1 and Nsa1 (Fatica et al., 2002; Sanghai et al., 2018). Similarly, our data indicate that the L1-stalk-interacting factors Nop2 and Nip7 as well as uL1 are already present in early nucleolar structures, although most likely in a more dynamic, unmoored state compared to late nucleolar particles (Figures 1C, 2A, and S2).

During maturation, rRNAs are extensively modified by small nucleolar RNA (snoRNA)-guided enzymatic complexes, resulting in pseudouridylation and 3′-OH methylation of ribose moieties. In addition, eight large subunit rRNA bases are modified by dedicated methyltransferases (Yang et al., 2016). Our quantitative MS data, in combination with known structural intermediates, allow us to place some of these catalytic activities into the 60S timeline (Figures 2A and S5). Components of the box H/ACA enzymatic complex (Cbf5, Gar1, and Nhp2), while most abundant in early, structurally uncharacterized intermediates and correlating most strongly with the box C/D components Nop1, Nop56, and Nop58 (Figure S5), are also detected in the Ssf1/Rrp15/Rrp14-containing structures (Figure 1D), suggesting that some snoRNA-guided pseudouridylation and 2′-*O*-methylation events may occur after some domains of the 60S rRNA have already folded. Because the H/ACA and C/D complexes are directed to modification sites by guide snoRNA, this suggests that rRNA domains III and IV, which are not ordered in these structures, may still be accessible to snoRNA-mediated modification. Our data also associate the activities of three base-modifying methyltransferases with specific maturation intermediates. Bmt2 and Rcm1, which our timeline associates with late nucleolar intermediates (after Ssf1 engagement, but before nucleolar release), catalyze the m^1A and m^5C methylation at rRNA residues 2142 and 2278, respectively, while Bmt5, associated with the earliest nucleoplasmic pre-60S particles (containing the RBFs Nog2 and Rpf2), methylates U2634 at the m^3 position (Figures 1D, 2A, and S5). The target nucleotides of these enzymes are located in rRNA domain IV, which is not ordered in the available nucleolar structures and therefore likely to be accessible for base modification.

Because nucleolar 60S intermediates are structurally well characterized, we used the catalytic function of Bmt2 and Rcm1 to validate our timeline. To test Bmt2 activity, we purified early nucleolar intermediates (Ssf1-TAP) and nucleoplasmic intermediates (Nog2-TAP). Primer extension assays of 25S rRNA extracted from these samples show that a band consistent with an m^1 methylation event at residue A2142 is present in the Nog2-containing intermediate, but not the Ssf1 intermediate (Figure 2B), consistent with our timeline, which predicts that this modification takes place during late nucleolar maturation. Similarly, we took advantage of a previously characterized Rcm1 mutation ($Rcm1^{C330A}$), which forms a covalent bond with its rRNA substrate and is toxic to cells (Sharma et al., 2013), allowing us to investigate the precise timing of Rcm1 engagement. We generated a yeast strain that

Author Manuscript Author Manuscript Author Manuscript Author Manuscript

allows for the estradiol-induced overexpression of Rcm1^{C330A} fused to a GFP-3x-Strep-tag and added secondary tags to either Ssf1 and Nop7 to differentiate between early and late nucleoplasmic intermediates (Figure 2C). Unlike the wild-type protein, Rcm1C330A is not exclusively located in the nucleolus, but also shows diffuse cytoplasmic distribution (Figure 2D), consistent with the idea that it remains covalently associated with 25S rRNA to disrupt proper 60S maturation. Tandem affinity purification using sequential immunoglobulin G (IgG) and Strep-Trap columns shows that the only intermediates retained over both columns, and thus containing trapped Rcm1, are the subset of Nop7-containing particles representing late nucleolar assembly steps, characterized by the presence of the RBFs Noc2, Noc3, and Spb1 (Figure 2E). Earlier Nop7-containing intermediates or intermediates containing Ssf1 flow unimpeded through the StrepTrap column, as no cross-linked Rcm1 is present at this maturation state (Figure 2E).

Our timeline also similarly suggests that Bmt5, which catalyzes the m3U modification at nucleotide 2634, engages the pre-60S after nucleolar release and Nog2 binding, but before 5S rRNP rotation and Rix1 binding (Figures 1D, 2A, and S5). Consistent with this timeline, cryo-EM reconstructions show that the loop containing U2634 is solvent exposed in the pre-rotation state but buried after 5S rRNA rearrangement (Wu et al., 2016; Zhou et al., 2019b), a process that may be promoted by the base modification.

Further, the distribution of the C2 processing factors Las1/Grc3 correlates strongly with the binding of Rix1/Rea1, allowing us to more narrowly define the timing of Las1 recruitment to the C2 site (Figures 2A and S5). This correlation between Las1 and the Rix1/Rea1 complex is consistent with the fact that Rix1-containing particles have distinct pools of particles with or without the ITS2 foot structure (Kater et al., 2020). Finally, we observe a close correlation between Ecm1 and the major export receptors Mex67/Mtr2, suggesting a functional link between these proteins in 60S nuclear export (Figures 2A and S5).

Timing of DEAD-box ATPases in 60S biogenesis

Perhaps the most prominent group of proteins “missing” from current cryo-EM structures are DEAD-box ATPases. While the precise role of these proteins in 60S biogenesis is unknown, they are thought to facilitate ATP-driven rRNA remodeling steps during ribosome assembly (Klinge and Woolford, 2019). Of the eight DEAD-box ATPases associated with 60S assembly, only Has1 has been modeled (Sanghai et al., 2018; Kater et al., 2017). However, Has1 has a structural, ATP-independent role in 60S biogenesis that is distinct from its catalytic function in 40S assembly (Dembowski et al., 2013). No high-resolution structural information exists for the remaining seven DEAD-box ATPases (Dbp6, Dbp7, Dbp9, Dbp10, Drs1, Mak5, and Spb4), although a tentative placement has been proposed for Spb4 (Sanghai et al., 2018; Kater et al., 2020) and rRNA regions contacting Mak5, Dbp10, and Spb4 have been defined by crosslinking and analysis of cDNAs (CRAC) experiments (Manikas et al., 2016; Brüning et al., 2018).

In this study, all eight DEAD-box proteins are reliably identified and quantified in our dataset (Figure 2F), allowing us to define the timing of their engagement with pre-60S particles. Dbp6 clusters with the earliest samples (Noc1, Rsa3), a placement that is consistent with previous studies showing that Dbp6 and Rsa3 form a stable complex that

Author Manuscript Author Manuscript Author Manuscript Author Manuscript

also includes Urb1/Urb2 and Nop8 (de la Cruz et al., 2004; Rosado et al., 2007). Dbp7, Dbp9 and Mak5, while already present in the Noc1 and Rsa3 particles, exhibit a broader distribution in our clustering pattern, extending into samples containing Ssf1 and Rrp14/15 (Figure 2F). Drs1 and Dbp10 are absent in the earliest clusters but feature prominently in the intermediate nucleolar samples (Figure 2F). Spb4 shows up last in our timeline and uniquely extends into pre-ribosomal particles containing Rix1, suggesting that Spb4 engagement occurs last among DEAD-box proteins (Figure 2F). DEAD-box function appears to be restricted to the nucleolus, with only low levels observed in nucleoplasmic or cytoplasmic particles. To obtain a more detailed picture of individual pairwise interactions between DEAD-box ATPases, we calculated individual abundance distribution correlations between each ATPase and all RBFs in our pool, selecting for the strongest correlations (Figure 2G; see STAR Methods for details). This analysis reveals a close abundance correlation between Dbp9, Mak5, and Mak11 and between Spb4 and Rrp17, reflecting the broad pattern discussed above and suggesting a role for Dbp9 and Mak5 in the early stages of nucleolar assembly and a late nucleolar role for Rrp17 (Oeffinger et al., 2009).

Implementation of a mono- and intralink filter (mi-filter) for AP-MS XL-MS data

To increase the reliability of our dataset and to enable the localization of previously unmapped or potentially additional RBFs with high confidence, we set out to filter out potentially falsepositive protein-protein interactions (PPIs). To date, false discovery rate (FDR) assessment in XL-MS has been addressed primarily through the optimization of scoring algorithms and the use of decoy databases (Beveridge et al., 2020; Walzthoeni et al., 2012; Fischer and Rappsilber, 2017; Gotze et al., 2019; Liu et al., 2015). Here, we took a different approach and used the expected distribution of monolinks, intralinks, and interlinks in our sample to filter out false-positive PPIs: If a protein is present at high enough quantities to be detectable by XL-MS, monolinks and intraprotein crosslinks will be generated at higher rates than interlinks (monolinks are formed when only one of the two active groups of the crosslinker is able to react with a lysine side chain) (Fursch et al., 2020). The mi-filter in our workflow stipulates that only proteins identified with at least one monolink or intraprotein crosslink within our dataset can be considered a bona fide interlink representing a legitimate PPI. This simple and intuitive filtering has a dramatic effect on our analysis. Using the Rix1 dataset as an example, a “standard” filter setting relying on one identified high-confidence crosslink per unique crosslinking site results in high FDRs, in particular for interprotein crosslinks (Figures 3A, 3D, 3G, and 3J). A more stringent filter setting relying on two independently identified high-confidence crosslinks improves the overall FDR to ~4%, a 7.5% reduction, but still results in a high percentage of unreliable interlinks and an overall low degree of confidence in individual PPIs (Figures 3B, 3E, 3H, and 3K). Application of the mi-filter, however, results in a dramatically improved overall FDR of <0.5%, and most striking, yields a near-100-fold improvement in the FDR for interprotein crosslinks (Figures 3C, 3F, 3I, and 3L). By applying the mi-filter to our complete crosslink dataset, the interlink FDR is improved to <0.4%, ensuring that the filtered PPIs can be mapped with great confidence (Figures 3M-3O).

Author Manuscript Author Manuscript Author Manuscript Author Manuscript

A database of high-confidence interlinks in 60S biogenesis intermediates

Our final crosslink dataset, after application of the mi-filter, consists of >60,000 mono- and crosslinks, with 2,844 inter-protein crosslinks among 145 individual proteins (Table S2: “Crosslink dataset of 60S pre-ribosomal particles”). 71 of these 145 are r-proteins of the large or small subunit (including homologous r-proteins), and another 50 belong to the structurally characterized RBFs (46 60S factors and 4 90S/40S factors). Only 7 RBFs known to be present in pre-60S intermediates are not represented by an interlink in our database (Tif6, Bud20, Sdo1, Ria1, Reh1, Mak16, and Rtc3). The remaining 352 interlinks involve 24 proteins with currently unknown localization. To visualize the sites of action of these remaining RBFs, we overlaid crosslink networks on the outlines of cryo-EM structures of pre-ribosomal particles, choosing the most appropriate structural scaffold, although some datasets, notably Cic1, span diverse structural intermediates (Figures 2A, 4, and S7); for an overview of the highlighted regions, see Figure S6). The 22 RBFs with previously unknown localization as well as 2 candidate biogenesis factors are shown together in Figure 5A.

Identification and localization of Tma16, Las1/Grc3, Ecm1, and Noc2

While our database will aid future interpretation of cryo-EM maps of 60S structural intermediates, specific interactions identified in our interlinks can already be used to map certain RBFs to 60S structural intermediates. Of the 9 candidate biogenesis factors identified in our quantitative analysis, only 2, Tma16 and Stm1, are also represented in our interprotein crosslink library. In total, 5 interprotein crosslinks between the N-terminal part of Tma16 and Rei1 and 5 interlinks between the C-terminal region of Tma16 and uL18 were identified (Table S2: “Number of interlinks for mapping”) in pre-ribosomal particles purified with affinity-tagged Arx1 (Figure S7H) and Lsg1 (Figure 4D). In our quantitative MS analysis, Tma16 exhibits an abundance pattern that is most similar to the Arx1/Alb1 complex (data not shown) across the Cic1, Rix1, Nop12, Nog2, Arx1, and Lsg1 pulldowns (Figure S4). These data point to Tma16 as an additional pre60S cytoplasmic RBF. uL18 and Rei1 are located quite distantly from each other on the surface of the pre-60S and engage opposite termini of Tma16, suggesting an extended conformation for this factor on the 60S surface.

During ribosome biogenesis, ITS2 removal is initiated by Las1-mediated cleavage at the C2 site within ITS2, followed by phosphorylation of the resulting 5′-hydroxyl product on the 25S rRNA by the Grc3 polynucleotide kinase (Fromm et al., 2017; Gasse et al., 2015; Pilion et al., 2019). In our interlink dataset, we map an interaction between Grc3 and the structurally uncharacterized C-terminal domain of Cic1 in pre-ribosomal particles purified with affinity-tagged Rix1 (Figure 4B) and Nog2 (Figures 4C and 5B). Pearson correlation analysis based on protein abundance in the different pre-ribosomal particles shows that the Las1/Grc3 complex correlates strongly with the Rix1/Rea1 complex (Figure S5), which is in line with the structural observation that pre-60S particles containing Rix1 and Rea1 can be reconstructed both with and without a foot structure (Kater et al., 2020). The correlated recruitment of the Rix1/Rea1 complex and Las1/Grc3 hints at a possible coordination between Rix1 complex binding and ITS2 processing.

Nuclear export of pre-60S particles is mediated by the export factors Arx1, Mex67-Mtr2, Nmd3, and Ecm1. These factors have overlapping, non-redundant roles in pre-60S export

Author Manuscript Author Manuscript Author Manuscript Author Manuscript

(Yao et al., 2010). While structural information is available for the other export factors, Ecm1, which binds to nucleoporins and shuttles between the nucleus and the cytoplasm, has not been observed in any cryo-EM reconstruction to date. Ecm1 is abundantly featured in our interlink dataset, with a total of 68 interprotein crosslinks between Ecm1, uL2, and eL43 found in the Nop12, Nog2, Arx1, and Lsg1 datasets and 3 crosslinks to Nog2 exclusively observed in the Nog2 dataset (Figures 4C, 4D, 5C, and S7; Table S2: “Crosslink dataset of DEAD-box ATPases and previously unmapped RBFs”). Mapping of these interacting residues onto late nuclear pre-60S particles implies that Ecm1 binds 60S after the removal of Rsa4 by Rea1, but before the release of the GTPase Nog2, because this is the only structural intermediate in which Nog2 is accessible for crosslinking with Ecm1 (Figure 5C) (Zhou et al., 2019b). In our MS quantification analysis, Ecm1 correlates strongly with the Mex67 and Mtr2 abundance pattern within late nucleoplasmic and cytoplasmic intermediates (Figure S5), implying a concerted engagement of pre-60S particles by these export factors.

Noc2 is an unusual pre-60S RBF, forming two distinct complexes (Noc1/Noc2 and Noc3/Noc2) that act at different stages of maturation. Noc3 and Noc1 share a conserved Noc motif that likely mediates their interaction with Noc2 (Milkereit et al., 2001). Accordingly, while the abundance of Noc1 and Noc3 is limited to very early and late nucleolar intermediates, respectively, Noc2 shows a bimodal distribution that matches the presence of Noc1 and Noc3, but not the intervening pre-60S intermediates (Figures 1C and 1D). Independently, we detect 10 interlinks between Noc1 and Noc2, all from a particle pool purified with tagged Noc1 (Figure S7; Table S2). The Noc3/Noc2 interaction is represented by 67 independent crosslinks, all mapping to late nucleolar samples. This pattern is consistent with 2 independent pre-60S engagements by Noc2, mediated by distinct dimerization partners. In late nucleolar samples, Noc2 is also associated with Brx1 (4 interlinks) and Nip7 (12 interlinks). Mapping these residues (or their closest modeled residue neighbors) onto the structure of late nucleolar 60S substrates shows that they triangulate around an area of unassigned density above Noc3 (Figure 5D). This density is consistent with the helical repeats predicted to occur within Noc2 (Milkereit et al., 2001). Because all crosslinks involve residues within the last 110 residues of Noc2, we propose that the Noc2 helical repeats extend away from Noc3 in a C- to N-terminal direction. Our crosslinking database also contains interactions between the methyltransferase Rcm1 and YBL028C and between the Box H/ACA snoRNP component Cbf5 and eL19 (Figure 5E), consistent with the abundance patterns of these proteins in our quantitative MS analysis (Figures 1D and 2A).

The Ck2 complex engages early 60S biogenesis intermediates

The heterotetrameric casein kinase 2 (Ck2) complex has a central role in cell growth and proliferation (Kos-Braun et al., 2017). Ck2 is a component of the CURI complex and is associated with pre-40S intermediates (Krogan et al., 2004). More recently, Ck2 activity was found to trigger a switch in ITS1 processing during stress responses that results in the disruption of normal 60S biogenesis (Kos-Braun et al., 2017). Our data suggest that Ck2 involvement in 60S ribosome biogenesis involves a physical interaction with early nucleolar pre-60S intermediates. All 4 subunits of Ck2 show a similar protein abundance pattern in pre-ribosomal particles purified with affinity-tagged Ssf1, Nsa1, Nop16, Ytm1, Cic1, and Noc1 (Figure 6A). In addition, we find 2 high-confidence inter-protein crosslinks

Author Manuscript Author Manuscript Author Manuscript Author Manuscript

between Cka1 (CSK21) and Puf6 in both Noc1 and Nop16 samples (Figures S7A and S7D). To confirm the link between Ck2 and the large subunit, we carried out a full quantitative and XL-MS analysis of intermediates using affinity-tagged Cka1 (CSK21). As expected, a clustering analysis shows that Cka1-associated RBFs are most similar to those associated with early nucleolar intermediates. In addition, identified interprotein crosslinks between Cka1 and large subunit RPs and RBFs together with mono- and intralinks among various proteins of the pre-60S foot structure and within Ssf1/Rrp15/Rrp14, Brx1/Ebp2, and Mak16/Rpf1/Nsa1 suggest a physical interaction between the Ck2 complex and early nucleolar pre-60S structures (Table S2: “Cka1 reciprocal pulldown”). Correlations from our quantitative MS data (Figure 6B) as well as interlinks and known physical interactions allow us to generate an extensive interaction map involving Ck2 (Figure 6C). This interactome offers a framework to understand the role and timing of Ck2 engagement in 60S maturation as several unmapped factors, such as Puf6/Loc1, Fpr3/4, and the DEAD-box ATPases Drs1, Mak5, and Dbp9, are connected to Ck2 and may be linked to its function during early nucleolar 60S maturation.

Localization of the DEAD-box ATPases Dbp9 and Dbp10

Except for Dbp6 and Dbp7, all of the DEAD-box ATPases involved in 60S biogenesis and identified in our MS quantification are represented in our crosslinking dataset (Figure 5A). Dbp9, Drs1, and Mak5 are contained in the interactome around Ck2, forming interlinks with uL6, Ytm1, and Puf6, respectively (Figure 6). Drs1 engages the Ytm1 β-propeller while it is still loosely tethered to the pre-60S core, making precise mapping of Drs1 impossible. Similarly, Mak5 is linked to Puf6, which has not been identified in any cryo-EM maps. Dbp9, however, forms a link between a loop insertion in its N-terminal RecA domain and uL6. Structures of nucleolar intermediates showed that uL6 binds the pre-60S core after domain VI docks onto the core (Figure 7A) (Kater et al., 2017; Sanghai et al., 2018). The intermediate immediately preceding uL6 binding is characterized by the presence of Mak11, while uL6 is necessary for the binding of the Nog1 GTPase domain, Mrt4, and Nsa2. The timing of uL6 binding and the absence of Dbp9 in later nucleolar particles is indicative of a narrow time window for Dbp9 to perform its catalytic function–after uL6 binding, but before the release of RBFs Ssf1, Rrp14, and Rrp15.

Our interlink database also provides extensive positional information about the DEAD-box proteins Dbp10 and Spb4 that engage late nucleolar 60S intermediates. Our Spb4 crosslinks confirm the assignment of Spb4 to a distinct, bilobed feature in the late nucleolar cryo-EM maps next to eL19, eL30, and Ytm1 (Sanghai et al., 2018; Kater et al., 2020) (Figure 5F). Spb4 binding is preceded in our timeline by Dbp10. A total of 65 interlinks associate Dbp10 with the RBFs Nog1 (3 links), Nop2 (2 links), Nsa2 (47 links), and Noc3 (13 links). On Dbp10, the residues proximal to Nog1, Nop2, and Nsa2 are located in the C-terminal extension of Dbp10, suggesting that this segment binds pre-60S particles in the cleft between Nop2 and Nog1 (Figure 7B). The link to Noc3 is located within the N-terminal RecA domain, placing the enzymatic core of the protein near the binding site of the N-terminal methyltransferase domain of Spb1 (Spb1-MT). CRAC experiments identified rRNA helices h89–h92 and h64 as Dbp10-interacting regions (Manikas et al., 2016). In the structure of a late nucleolar 60S intermediate, these rRNA elements are engaged by the MT

Author Manuscript Author Manuscript Author Manuscript Author Manuscript

domain of Spb1 and are not accessible for Dbp10 binding (Kater et al., 2017). This suggests that Dbp10 binds the 60S before Spb1-MT and Spb4 binding, in line with our quantitative MS data. In fact, by engaging helices h89–h92 and h64, Dbp10 blocks these rRNA elements from being available to bind the Spb1-MT domain. Further studies will be needed to define the mechanistic details of the sequential engagement of these RNA elements by Dbp10 and Spb1-MT.

DISCUSSION

Understanding the assembly process of large molecular complexes remains a challenging problem. By integrating both quantitative and structural proteomics data with atomic resolution models, we generated a comprehensive timeline for nearly all known RBFs in large ribosomal subunit biogenesis. We validate the predictive power of our timeline by showing that the rRNA-modifying activity of two methyltransferases, Bmt2 and Rcm1, occurs precisely at the 60S maturation stage indicated by our timeline. Our high-confidence interlink dataset reliably recapitulated the positioning information for structurally characterized 60S RBFs and reveals positioning information for 22 known but currently structurally uncharacterized 60S AFs.

Combining our quantitative and positional MS data with available cryo-EM structures of pre-60S ribosomal intermediates allowed us to precisely map interaction areas for the RBFs Noc2, Las1/Grc3, and Ecm1 during key steps of 60S maturation: Interlinks to Noc2 associate it unambiguously with a series of helical repeats above Noc3 in late nucleolar structures. Our analysis shows that the ITS2 processing complex Las1/Grc3 is recruited to early nucleoplasmic 60S particles at the same time as the Rix1/Rea1 complex, suggesting a coordination between ITS2 removal, 5S rRNA rotation, and Rsa4 removal. Ecm1, one of several 60S export factors, is closely linked with the presence of the major export receptor, Mex67/Mtr2, suggesting that the assembly of an export-competent 60S particle occurs in a concerted manner.

While previous studies have identified components of the heterotetrameric Ck2 casein kinase complex in preparations of ribosomal intermediates, our data suggest an extensive interaction network between this regulatory complex and a cluster of nucleolar RBFs. The distribution of Ck2 subunits in our timeline is consistent with the engagement of the earliest pre-60S intermediates. Previous studies revealed a role for Ck2 within the CURI complex, composed of pre-40S AFs Utp22 and Rrp7 and the transcription factor Ifh1. CURI is proposed to play a role in coordinating the transcription of rRNA and r-proteins in response to external stress (Rudra et al., 2007). In this model, when rRNA transcription is reduced, free Utp22/Rrp7/Ck2 is able to bind Ifh1, reducing its ability to promote r-protein gene transcription. More recently, Kos-Braun et al. (2017) showed that under stress conditions, a switch in rRNA processing leads to the formation of “dead-end” pre-40S and pre-60S ribosomal intermediates. The switch between these sites is dependent on Ck2, leading to suggestions that Ck2 may not only help coordinate ribosome biogenesis at the level of transcription but also provide a feedback mechanism to convey defects in ribosomal assembly to the rRNA and r-protein transcriptional machinery (de la Cruz et al., 2018). Our data indicate a role for Ck2 in early nucleolar 60S maturation that is independent of Utp22

Author Manuscript Author Manuscript Author Manuscript Author Manuscript

and Rrp7, even though these results warrant further experimental validation. The consistent presence of Ck2 in multiple early 40S and 60S assembly intermediates makes it an attractive candidate to coordinate a global response to cellular stress that involves both transcriptional regulation of rRNA and r-proteins and pausing the assembly of new ribosomes. Systematic studies of Ck2 substrates in mammalian cells identify the human homologs of 2 of our proposed 60S Ck2 interaction partners, Nop2 and Rrp1, as potential Ck2 phosphorylation targets (Rusin et al., 2017). More important, our data, including the purification of bona fide 60S intermediates with affinity-tagged Cka1, suggest that it is not just the catalytic activity of Ck2 that is essential for its role in maintaining biogenesis, but that similar to its engagement with Utp22 and Rrp7, Ck2 is physically associated with a subset of nucleolar ribosome intermediates during early 60S maturation.

To date, the most elusive RBFs in 60S biogenesis have been the 7 DEAD-box ATPases whose catalytic activity is essential for nucleolar 60S maturation. We identify all of these enzymes in our quantitative dataset and all but Dbp6 and Dbp7 in our crosslinking analysis, defining a timeline of 60S engagement for these proteins: Dbp6 → Dbp7 → Mak5 → Dbp9 → Drs1 → Dbp10 → Has1 → Spb4. Dbp6, which acts within a complex composed of the factors Urb1, Urb2, Rsa3, and Nop8, engages the emerging 60S particle just as ITS1 is being processed and the 35S rRNA separated into the 20S and 27S fragments. Mak5 and Dbp9 are part of our Ck2 interaction cluster and may play a role in organizing the docking of rRNA domain VI to the 60S core. Because of its direct interaction with uL6 and the fact that the timing of uL6 incorporation into the pre-60S is known from cryo-EM structures of 60S intermediates, we propose a function for Dbp9 in promoting rRNA rearrangements to guide the assembly of the Nog1/Nsa2/Mrt4 region within nucleolar pre-60S intermediates. Similarly, an extensive network of interlinks defines the placement of Dbp10 and establishes that the binding of Dbp10 and that of the methyltransferase domain of Spb1 must occur sequentially. Both Dbp10 and Spb4 are associated with rRNA domain IV, the last segment of the rRNA to dock against the pre-60S core and may remodel this rRNA region to chaperone its folding and ordered assembly.

In summary, in this work we successfully applied quantitative proteomics and XL-MS together with large-scale biochemical enrichment of pre-ribosomal particles as a stand-alone technique to characterize transient and dynamic interactions across the full landscape of 60S pre-ribosomal particles. Integration of our MS data with available cryo-EM structures allowed us to comprehensively map RBFs involved in 60S ribosome biogenesis, providing important new insights into the timeline of Ck2 involvement and DEAD-box ATPase function in 60S biogenesis. Our high-confidence large-scale crosslinking interaction map and detailed timeline represent an essential resource for future structural and functional studies of 60S ribosome biogenesis.

Limitations of the study

Eukaryotic ribosome biogenesis is facilitated and regulated by numerous RBFs. In this study, we use quantitative proteomics and XL-MS data from an extensive set of pre-ribosomal particles to derive a comprehensive and time-resolved interaction map of RBF engagement during 60S maturation in the yeast *S. cerevisiae*.

Author Manuscript Author Manuscript Author Manuscript Author Manuscript

Agreement with known intermediate structures and validation experiments speak to the overall robustness of our RBF engagement timeline, but the precision of individual RBF timelines will vary given that MS is an ensemble technology. Similarly, the excellent overall quality of our XL-MS dataset does not preclude the presence of individual false-positive crosslinks in our dataset. Finally, within our quantitative analysis there is a continuum between previously unknown, bona fide, low-abundance RBFs and residual contaminants in our samples. Follow-up studies will be required to determine which of these borderline factors may play either direct or regulatory roles in 60S assembly.

STAR★METHODS

RESOURCE AVAILABILITY

Lead contact—Further information and requests for resources and reagents should be directed to the lead contact (florian.stengel@uni-konstanz.de).

Materials availability—• Detailed information on the yeast strains generated in this study are available from the lead contact upon request.

Data and code availability

- Original mass spectrometric data have been deposited at the ProteomeXchange Consortium via PRIDE partner repository and are publicly available as of the date of publication. Accession details are listed in the key resources table.
- This paper does not report original code.
- Any additional information required to reanalyze the data reported in this paper is available from the lead contact upon request.

EXPERIMENTAL MODEL AND SUBJECT DETAILS

Yeast strains—Saccharomyces cerevisiae BY4741 (MATa: his3Δ1 leu2Δ0 met15Δ0 ura3Δ0) strains used in this study and mutant strains generated in this study are listed in the key resources table.

METHOD DETAILS

Affinity enrichment of assembly intermediates—Ribosome assembly intermediates were purified from *S. cerevisiae* BY4741 cells by tandem affinity purification (TAP). 12 different *S. cerevisiae* BY4741 strains with the TAP-tagged bait proteins Noc1, Rsa3, Ssf1, Nop16, Ytm1, Nsa1, Cic1, Rix1, Nop12, Nog2, Arx1 and Lsg1 were used for the affinity purification of ribosome assembly intermediates, each performed in biological triplicates (i.e. pulldowns from independently grown yeast cultures). A wild type *S. cerevisiae* BY4741 strain without any TAP-tagged protein served as control for unspecific binding. In addition, a reciprocal affinity purification with TAP-tagged Cka1 was performed.

For each affinity purification, 12 L YPD medium (2 % (w/v) peptone, 1% (w/v) yeast extract, 2 % (w/v) glucose, 0.002 % (w/v) adenine) were inoculated from 300 ml over-night culture with an OD_{600} of 0.1 and grown at 30°C and 130 rpm to OD_{600} = 0.8 – 1.0.

Author Manuscript Author Manuscript Author Manuscript Author Manuscript

Cells were harvested by centrifugation at 4300 x g and 4°C for 12 min. Cell pellets were resuspended in 80 ml cold lysis buffer (LB-P, 50 mM HEPES pH 7.4, 100 mM KCl, 1.5 mM $MgCl_2$, 0.1 % (v/v) NP-40, 5 % (v/v) glycerol, pefabloc 1:100, aprotinin/leupeptin 1:1000) and centrifuged at 4000 x g and 4°C for 5 min. Washed cell pellets were resuspended in 20 ml LB-P and dripped into liquid nitrogen. Frozen droplets of cell suspension were stored at −80°C until milling in a pre-cooled Retsch® ball mill MM400 at 30 Hz for 2× 60s. 150 ml ice cold LB-P was added to the frozen cell powder which was thawed on a rolling mixer at 4°C. Cell debris was separated from the lysate by centrifugation at 30000 x g and 4°C for 20 min. The lysate was incubated with 1.2 ml equilibrated IgG sepharose beads (GE Healthcare) at 4°C for 3 h. IgG beads were washed 3x with LB-P and 1x with LB-DTT (50 mM HEPES pH 7.4, 100 mM KCl, 1.5 mM $MgCl_2$, 0.1 % (v/v) NP-40, 5 % (v/v) glycerol, 1 mM DTT). IgG beads were loaded onto a 5 mL Polyprep® column using 3× 10 mL LB-DTT. The column was closed and IgG beads were incubated in 4.5 mL LB-DTT with 175 µl TEV protease (produced inhouse, 1.5 µg/µL in 10 % glycerol) at 4°C over-night on a rolling incubator. IgG eluate was incubated with 1 mL equilibrated calmodulin affinity resin (Agilent) in 15 mL LB-$CaCl_2$ (50 mM HEPES pH 7.4, 100 mM KCl, 1.5 mM $MgCl_2$, 0.02 % (v/v) NP-40, 5 % (v/v) glycerol, 2 mM $CaCl_2$) at a final $CaCl_2$ concentration of 2 mM on a rolling mixer at 4°C for 3 h. Calmodulin beads were loaded onto a 5 mL Polyprep® column using 2x20 mL LB-$CaCl_2$ and washed with 1x10 mL LB-$CaCl_2$. The column was closed and calmodulin beads were incubated with 550 µL LB-EGTA (50 mM HEPES pH 7.4, 100 mM KCl, 1.5 mM $MgCl_2$, 0.01 % (v/v) NP-40, 5 % (v/v) glycerol, 5 mM EGTA) for 20 min at 4°C on a rolling incubator. The eluate was collected and the elution was repeated 3x with 450 µL LB-EGTA. Eluates 1 –4 were concentrated using an Amicon® Ultra 10 K 0.5 mL filter (Merck Millipore) and the buffer was exchanged to a final volume of ca. 100 µl crosslinking buffer (20 mM HEPES pH 8.3, 5 mM $MgCl_2$).

Chemical crosslinking of assembly intermediates—Chemical crosslinking and subsequent analysis were carried out essentially as described previously (Leitner et al., 2014). In short, the isotopically labeled crosslinking reagent disuccinimidyl suberate d0/d12 (DSS-H12/D12, Creativemolecules Inc.) was dissolved in N,N-Dimethylformamide (DMF, Sigma) and purified ribosome assembly intermediates were incubated with DSS-H12/D12 at a final concentration of 1.5 mM for 30 min at 30°C while shaking at 650 rpm in a Thermomixer (Eppendorf). The reaction was subsequently quenched with ammonium bicarbonate at a final concentration of 50 mM for 10 min at 30°C and 650 rpm. Crosslinked samples were stored at −20°C overnight.

Fractionation and enrichment of crosslinked peptides—Crosslinked samples were dried (Eppendorf, Concentrator plus), resuspended in 100 µl 8M Urea, reduced, alkylated, and digested with trypsin (Promega). Digested peptides were separated from the solution and retained by a solid phase extraction system (SepPak, Waters). Crosslinked peptides were enriched by size exclusion chromatography using an ÄKTAmicro chromatography system (GE Healthcare) equipped with a Superdex™ Peptide 3.2/30 column (column volume = 2.4 ml). Fractions were collected in 100 µl units and analyzed by LC-MS/MS. For each crosslinked sample three fractions were measured in technical duplicates. The elution fractions 1.0-1.1, 1.1-1.2 and 1.2-1.3 ml containing the largest peptides were pooled and

Author Manuscript Author Manuscript Author Manuscript Author Manuscript

the two elution fractions 1.3-1.4 ml and 1.4-1.5 ml were also analyzed by LC-MS/MS. Absorption levels at 215 nm of each fraction were used to normalize peptide amounts prior to LC-MS/MS analysis.

LC-MS/MS analysis—LC-MS/MS analysis was carried out on an Orbitrap Fusion Tribrid mass spectrometer (Thermo Electron, San Jose, CA). Peptides were separated on an EASY-nLC 1200 system (Thermo Scientific) at a flow rate of 300 nl/min over an 80 min gradient (5 % acetonitrile in 0.1 % formic acid for 4 min, 5 % - 35 % acetonitrile in 0.1% formic acid in 75 min, 35 % - 80 % acetonitrile in 1 min). Full scan mass spectra were acquired in the Orbitrap at a resolution of 120,000, a scan range of 400 - 1500 m/z, and a maximum injection time of 50 ms. Most intense precursor ions (intensity $\geq 5.0 \times 10^3$) with charge states 3 - 8 and monoisotopic peak determination set to 'peptide' were selected for MS/MS fragmentation by CID at 35 % collision energy in a data dependent mode. The duration for dynamic exclusion was set to 60 s. MS/MS spectra were analyzed in the Iontrap at a rapid scan rate.

Identification of crosslinked peptides—For the crosslink search, a database containing a total of 384 proteins was compiled including all 117 known r-proteins (including both alleles for homologous r-proteins which do not share 100 % sequence identity), all 81 assembly factors which are present in structures of pre-ribosomal particles as well as all 83 known assembly factors which have not been positioned yet (Woolford and Baserga, 2013). Additionally, the 82 proteins identified in this study as candidate RBFs were added to the database for the crosslink search. In the control pulldowns, which were performed from a wild type *S. cerevisiae* BY4741 strain without a TAP-tagged bait protein, 24 proteins were identified. 7 of these 24 proteins were r-proteins or known assembly factors and the remaining 17 proteins were added to the database for the crosslink search. Crosslinks to these 24 proteins were subtracted later during the analysis. In 4 select cases, where proteins could not be unambiguously identified because parts of the sequence could be matched to multiple proteins, additional sequences in order to allow unambiguous assignment were added to the database.

MS raw files were converted to centroid files and searched using *xQuest* in ion-tag mode. Crosslinks were exported as .tsv files with the filter settings deltaS < 0.95 and a max. ppm range from −5 to 5, containing all (non-unique) identifications.

Mapping of filtered crosslinks—Crosslink networks were visualized with xiNet (Combe et al., 2015) and mapped manually onto cryo-EM structures of pre-ribosomal particles. For a better overview, several binding regions of RBFs on the cryo-EM structures were highlighted (see Figure S6). The crosslink networks of the 'intermediate' 60S pre-ribosomal particles Nop16, Ytm1 and Cic1 were laid onto the PDB: 6ELZ, which was purified as state E sequentially by Rix1-TAP and Rpf2-Flag and contains the Ytm1 E80A mutant for impaired removing of the Erb1-Ytm1 complex by Rea1 (Kater et al., 2017). Crosslink networks of Ssf1 and Nsa1 pre-60S particles were laid onto the earlier state C (PDB: 6EM1). The crosslink networks of the 'intermediate to late' 60S pre-ribosomal particles Nop12, Nog2 and Arx1 were laid onto PDB: 3JCT, which was purified by Nog2 (Wu et al., 2016) and the Rix1 crosslink network was laid onto PDB: 6YLH purified by Rix1

Author Manuscript Author Manuscript Author Manuscript Author Manuscript

and Rea1 (Kater et al., 2020). The crosslink network of Lsg1 was laid onto PDB: 6RZZ, which was purified by Lsg1 (Kargas et al., 2019). All crosslink networks (excluding proteins containing only mono- or intralinks) can be seen in Figures 4 and S7.

Primer extension assay—Ribosome assembly intermediates were affinity purified as described using bait proteins Ssf1-TAP and Nog2-TAP. Ribosomal RNA of purified intermediates was precipitated by adding 2.5 volumes of ice-cold ethanol, followed by extraction and purification of 25S rRNA using the RNA Clean and Concentrator-25 Kit (Zymo Research) with the option to purify large RNAs (>200 nt). The primer extension assay was carried out essentially as described (Sharma et al., 2013). In short, 10 μM PAGE-purified DNA primer complementary to positions 2178-2201 of 25S rRNA was 5'-^{32}P-terminally labelled using 20 μCi ^{32}P-ATP (5000 Ci/mmol) and 20 units T4 polynucleotide kinase (Thermo Scientific) in 1x polynucleotide kinase buffer for 1 h at 37°C. The reaction was stopped by incubation at 95°C for 2 min and remaining ^{32}P-ATP was removed viaSephadex G-25 gel filtration. ^{32}P-labelled primer was diluted to 3 mM with non-labelled primer. 0.72 pmol of purified 25S rRNA was added to 0.18 pmol radioactively labelled primer in hybridization buffer (50 mM HEPES pH 7, 100 mM KCl) to a final volume of 10 μL. The primer/template mix was incubated at 90°C for 1 min before cooling over 10 min down to a temperature of 45°C. Then, 4 μL extension mix were added with a final concentration of 1 μM dNTPs and 5 mM DTT in 1x first strand buffer. The reaction was equilibrated to 42°C before 30 U Superscript reverse transcriptase III (Invitrogen) were added to start the extension reaction. The reaction was incubated for 30 min or 60 min at 42°C before stopping by adding 2x volumes of form-amide loading dye. 1.5 μL of each sample was subsequently loaded onto an 8 % urea-polyacrylamide gel with unreacted primer as control. The gel was run at 100W for 2-3 h and after transfer to Whatman paper exposed to a phosphoimager screen for 18 hrs and scanned on a Typhoon™ FLA9500 imager using the phosphoimager method.

Overexpression and purification of pre-ribosomes—For Rcm1 overexpression plasmids, full length wild-type *RCM1* or *rcm1^{C330A}* was cloned into a modified pRS406 plasmid under the control of a β-estradiol inducible system (Ottoz et al., 2014). Constructs were integrated into strain with C-terminally 3x-Strep-tagged *NOP7* or *SSF1* as a single copy, resulting in similar expression levels. Rcm1 was tagged with an N-terminal sfGFP–3xStrep–bdNEDD8–MYC tag. Starter cultures were grown overnight in YPD to saturation. The following morning 4L of YPD were inoculated from the starters to an OD_{600} of 0.1 and grown at 30°C to an OD_{600} of 0.8. Overexpression was induced for 1 hour by the addition of β-estradiol to a final concentration of 2 *μM*. Cells were harvested by centrifugation for 20 min at 4000 g, the pellets were washed in Ribo-buffer A (50 mM Bis-Tris-Propane KCl pH 8.0, 150 mM NaCl, 10 mM $MgCl_2$, 1 mM TCEP and 0.1% (w/v) NP-40) and centrifuged again for 10 min at 4000 g. Cell pellets were harvested and flash frozen in liquid nitrogen. Cryogenic lysis was done using a grinding ball mill (Fritsch Pulverisette 6). For purification of pre-ribosomes, 10 g of lysate are warmed to 4°C before addition of Ribo-buffer A supplemented with E64, pepstatin and PMSF. Lysate is cleared by centrifuging at 100,000 g for 30 min and loaded onto IgG Sepharose resin (Cytiva). Samples are washed with 10 column volumes of Ribo-buffer A followed by 10 column volumes of Ribo-buffer

Author Manuscript Author Manuscript Author Manuscript Author Manuscript

B (50 mM Bis-Tris-Propane KCl pH 8.0, 150 mM NaCl, 10 mM $MgCl_2$, 1 mM TCEP and 0.01% (w/v) NP-40). Protein-A tags were cleaved on-column using 3C protease and applied to a Strep-Tactin column (Cytiva), washed with 5 column volumes of Ribo-buffer B and eluted using bdNEDD8 protease before concentration on Amicon ultra 0.5 ml spin columns with a 100 kDa cutoff (Merck Millipore). The same procedure was performed for Tma16 purifications, except that the second purification step was performed in batch with Anti-FLAG-beads (Cytiva).

Microscopy—Strains were grown overnight in YPD to saturation, then diluted 20-fold into SC-Trp with β-estradiol to a final concentration of 2 μM for 1.5 hours. Yeast cells were mixed with low melting point agarose to limit motion while imaging and applied to a standard microscopy slide for live imaging using a Nikon Ti2-E equipped with a Yokogawa CSU-X1 spinning disk and a 100x NA = 1.49 oil objective. Samples were illuminated with a 488 nm solid state laser light source and images collected on an ORCA-FLASH 4.0 sCMOS camera. A single z-slice through the center of the cell was acquired for two fields of view in a single biological replicate. Image processing was performed using ImageJ (Collins, 2007; Schneider et al., 2012).

QUANTIFICATION AND STATISTICAL ANALYSIS

Label free quantification—Proteins were identified based on their non-crosslinked peptides and quantified in a label-free approach by MaxQuant (version 1.6.5.0.) using standard settings and the match between runs option (Hein et al., 2015). Detailed search parameters were deposited together with the raw files at PRIDE. As fasta database the *Saccharomyces cerevisiae* (strain ATCC 204508 / S288c) proteome with the proteome ID UP000002311 was downloaded from uniProt on 04.03.2019.

For the downstream analysis of the non-crosslinked proteomic data the Perseus platform (version 1.6.5.0.) was used (Tyanova et al., 2016b). In short, MaxQuant results were filtered for hits in the reverse database, for proteins which have been only identified by site and for potential contaminants. After log2(x) transformation of the LFQ values, proteins were considered to be reproducibly identified, if an LFQ value could be determined in all 3 biological replicates in at least one of the technical replicates of at least one purified pre-ribosomal particle. Missing LFQ values were imputed for the total matrix from a normal distribution (width = 0.3 and down shift = 1.8). In order to test for the variance of the determined LFQ values in the 3 biological replicates of each pre-ribosomal particle, an ANOVA significance test with the parameter s0 = 0 in combination with a permutation-based FDR estimation (FDR = 0.05) was applied. For the permutation-based FDR estimation, technical replicates were indicated and randomized together. As a negative control for non-specific binding during the purification of pre-ribosomal particles, a wild type yeast strain containing no TAP-tagged protein was used. If a protein was reproducibly identified with an LFQ value in all 3 biological replicates in at least one of the technical replicates of the negative control, this protein was not considered for further analysis.

The remaining 272 proteins were used to hierarchically cluster the different biological and technical replicates of purified pre-ribosomal particles based on their similarity in protein

Author Manuscript Author Manuscript Author Manuscript Author Manuscript

abundance by an L1 distance metric (Figure S1). Protein abundances are sorted by unbiased hierarchical clustering and are shown as Z-score normalized log2 transformed LFQ values ranging from ≤ −4.0 (white) to 0.0 (azure blue) to ≥ 2.5 (dark blue) from early to late assembly states. Interactors are additionally grouped into ‘early’ (red), ‘early-intermediate’ (orange), ‘intermediate’ (light blue), intermediate-late’ (light green) and ‘late’ (signal violet) proteins as well as proteins specific for one bait (shades of grey) (Figures 1B-1D, 2A, 2F, 6A, S2-S4, and S5B and Table S1).

For some specific subsets of the total of 272 quantified proteins (e.g. the DEAD-box ATPases and the 4 subunits of Ck2) an additional correlation analysis was carried out, where proteins that showed a similar abundance pattern over the different pre60S particles were identified. For this purpose, Z-score normalized log2 transformed LFQ values were averaged over the 6 replicate measurements for each of the 12 TAP-tagged bait proteins and a standard correlation coefficient (pearson) was calculated for any two pairs of the 272 proteins. Protein abundances are shown as Z-score normalized log2 transformed LFQ values ranging from ≤ −3.0 (white) to −0.5 (azure blue) to ≥ 2.0 (dark blue)(DEAD-box ATPases) orfrom ≤ −4.0 (white) to 0.0 (azure blue) to ≥ 2.5 (dark blue) (CK2). Here, proteins with a correlation coefficient ≥ 0.95 to any of the DEAD-box ATPases were considered to correlate (Figure 2G) and proteins with a correlation coefficient >0.85 to three out of the four subunits of the casein kinase Ck2 complex, one of which had to be > 0.9, were considered to correlate (Figure 6B).

Mono- and intralink filter—Subsequent filtering and analysis of *xQuest* results was done with python / pandas and jupyter notebook. The FDR was calculated as number of decoys / (number of decoys + number of hits). Please note that crosslinked peptides containing at least 1 decoy_peptide were considered as decoys. Three different filter settings were compared in this study. A “standard” filter setting relying on one identified high-confidence crosslink per unique crosslinking site (uxID) (ld-Score ≥ 25, uxID n=1), a more stringent filter setting relying on two independently identified high-confidence crosslinks per uxID (over all AP-MS datasets) (ld-Score ≥ 25, uxID n=2) and the “final” setting, which was also the final setting used for our analysis, which additionally uses a mono- and intralink filter (mi-filter) which requires that for each protein involved in an interprotein crosslink also at least one mono- or intralink had to be detected in one of the three biological replicates (Id-Score ≥ 25, uxID n=2 , mi-filter). After filtering, non-specific crosslinks and non-specific proteins identified in the negative control pulldown (without a bait protein) were subtracted from the datasets. Here, 24 unspecific binders were identified based on non-crosslinked peptides and 7 via crosslinks and therefore subtracted from the datasets.

The final dataset, after filtering and subtraction of unspecific crosslinks/ proteins identified in the negative control, contained 43205 monolinks (FDR = 0.00138) consisting of 1362 unique monolink sites (FDR = 0.00365), 15802 intraprotein crosslinks (FDR = 0.00327) consisting of 947 unique intralink sites (FDR=0.002107) and 2844 interprotein crosslinks (FDR = 0.00385) consisting of 290 unique crosslinking sites (FDR = 0.0136) and 145 proteins.

Author Manuscript Author Manuscript Author Manuscript Author Manuscript

Filtering of peptides for Cka1 pulldown—The *xQuest* results of each biological replicate were exported from the results viewer as .tsv files containing all (non-unique) identifications with the filter settings deltaS < 0.95 and a max. ppm range from −5 to 5. Subsequent filtering and analysis were done with python / pandas and jupyter notebook. Only interprotein crosslinks between proteins, which were identified with at least 1 mono-, intrapeptide- or intraproteinlink with an ld-Score ≥ 25, were considered for further analysis.

Supplementary Material

Refer to Web version on PubMed Central for supplementary material.

ACKNOWLEDGMENTS

We thank Christoph Hanselka for help with reviewing the crosslink database; Antonia Vogel, Niginia Borlinghaus, and Philipp Schmid for help with the affinity enrichments; Patrick Arner, Cornelia Hauser, Melanie Henkel, and Luisa Huber for help with the primer extension assay; Kai-Michael Kammer and Robin Marzucca for help with python/pandas scripts for FDR calculation and data analysis; and Christine Weirich for help with live imaging and critical reading of the manuscript. We thank the lab of Elke Deuerling for *S. cerevisiae* strains Arx1-TAP, Lsg1-TAP, and wild-type BY4741. This work was supported by the German Research Foundation Collaborative Research Centre 969 (Project A06). J.P.E. was supported by the Cancer Prevention and Research Institute of Texas (RR150074), the Welch Foundation (I-1897), the UTSW Endowed Scholars Fund, and the National Institutes of Health (GM135617-01). F.S. is grateful for funding from the Emmy Noether Programme of the German Research Foundation (STE 2517/1-1).

REFERENCES

Barandun J, Chaker-Margot M, Hunziker M, Molloy KR, Chait BT, and Klinge S (2017). The complete structure of the small-subunit processome. Nat. Struct. Mol. Biol 24, 944–953. [PubMed: 28945246]

Beveridge R, Stadlmann J, Penninger JM, and Mechtler K (2020). A synthetic peptide library for benchmarking crosslinking-mass spectrometry search engines for proteins and protein complexes. Nat. Commun 11, 742. [PubMed: 32029734]

Brachmann CB, Davies A, Cost GJ, Caputo E, Li J, Hieter P, and Boeke JD (1998). Designer deletion strains derived from *Saccharomyces cerevisiae* S288C: A useful set of strains and plasmids for PCR-mediated gene disruption and other applications. Yeast 14, 115–132. [PubMed: 9483801]

Brüning L, Hackert P, Martin R, Davila Gallesio J, Aquino GRR, Urlaub H, Sloan KE, and Bohnsack MT (2018). RNA helicases mediate structural transitions and compositional changes in pre-ribosomal complexes. Nat. Commun 9, 5383. [PubMed: 30568249]

Cheng J, Kellner N, Berninghausen O, Hurt E, and Beckmann R (2017). 3.2-A-resolution structure of the 90S preribosome before A1 pre-rRNA cleavage. Nat. Struct. Mol. Biol 24, 954–964. [PubMed: 28967883]

Cherry JM, Hong EL, Amundsen C, Balakrishnan R, Binkley G, Chan ET, Christie KR, Costanzo MC, Dwight SS, Engel SR, et al. (2012). Saccharomyces Genome Database: the genomics resource of budding yeast. Nucleic Acids Res. 40, D700–D705. [PubMed: 22110037]

Collins TJ (2007). ImageJ for microscopy. Biotechniques 43, 25–30.

Combe CW, Fischer L, and Rappsilber J (2015). xiNET: cross-link network maps with residue resolution. Mol. Cell. Proteomics 14, 1137–1147. [PubMed: 25648531]

de la Cruz J, Gómez-Herreros F, Rodríguez-Galán O, Begley V, de la Cruz Muñoz-Centeno M, and Chávez S (2018). Feedback regulation of ribosome assembly. Curr. Genet. 64, 393–404. [PubMed: 29022131]

de la Cruz J, Lacombe T, Deloche O, Linder P, and Kressler D (2004). The putative RNA helicase Dbp6p functionally interacts with Rpl3p, Nop8p and the novel trans-acting Factor Rsa3p during biogenesis of 60S ribosomal subunits in Saccharomyces cerevisiae. Genetics 166, 1687–1699. [PubMed: 15126390]

Author Manuscript Author Manuscript Author Manuscript Author Manuscript

Dembowski JA, Kuo B, and Woolford JL JR. (2013). Has1 regulates consecutive maturation and processing steps for assembly of 60S ribosomal subunits. Nucleic Acids Res. 41, 7889–7904. [PubMed: 23788678]

Eppens NA, Faber AW, Rondaij M, Jahangir RS, van Hemert S, Vos JC, Venema J, and Raué HA (2002). Deletions in the S1 domain of Rrp5p cause processing at a novel site in ITS1 of yeast pre-rRNA that depends on Rex4p. Nucleic Acids Res. 30, 4222–231. [PubMed: 12364601]

Fatica A, Cronshaw AD, Dlakić M, and Tollervey D (2002). Ssf1p prevents premature processing of an early pre-60S ribosomal particle. Mol. Cell 9, 341–351. [PubMed: 11864607]

Fischer L, and Rappsilber J (2017). Quirks of error estimation in cross-linking/mass spectrometry. Anal. Chem 89, 3829–3833. [PubMed: 28267312]

Fleischer TC, Weaver CM, McAfee KJ, Jennings JL, and Link AJ (2006). Systematic identification and functional screens of uncharacterized proteins associated with eukaryotic ribosomal complexes. Genes Dev. 20, 1294–1307. [PubMed: 16702403]

Fromm L, Falk S, Flemming D, Schuller JM, Thoms M, Conti E, and Hurt E (2017). Reconstitution of the complete pathway of ITS2 processing at the pre-ribosome. Nat. Commun 8, 1787. [PubMed: 29176610]

Fursch J, Kammer KM, Kreft SG, Beck M, and Stengel F (2020). Proteome-Wide structural probing of low-abundant protein interactions by crosslinking mass spectrometry. Anal. Chem 92, 4016–4022. [PubMed: 32011863]

Gamalinda M, Ohmayer U, Jakovljevic J, Kumcuoglu B, Woolford J, Mbom B, Lin L, and Woolford JL JR. (2014). A hierarchical model for assembly of eukaryotic 60S ribosomal subunit domains. Genes Dev. 28, 198–210. [PubMed: 24449272]

Gasse L, Flemming D, and Hurt E (2015). Coordinated ribosomal ITS2 RNA processing by the Las1 complex integrating endonuclease, polynucleotide kinase, and exonuclease activities. Mol. Cell 60, 808–815. [PubMed: 26638174]

Ghaemmaghami S, Huh W-K, Bower K, Howson RW, Belle A, Dephoure N, O'Shea EK, and Weissman JS (2003). Global analysis of protein expression in yeast. Nature 425, 737–741. [PubMed: 14562106]

Gotze M, Iacobucci C, Ihling CH, and Sinz A (2019). A simple cross-linking/mass spectrometry workflow for studying system-wide protein interactions. Anal. Chem 91, 10236–10244. [PubMed: 31283178]

Hein MY, Hubner NC, Poser I, Cox J, Nagaraj N, Toyoda Y, Gak IA, Weisswange I, Mansfeld J, Buchholz F, et al. (2015). A human interactome in three quantitative dimensions organized by stoichiometries and abundances. Cell 163, 712–723. [PubMed: 26496610]

Kargas V, Castro-Hartmann P, Escudero-Urquijo N, Dent K, Hilcenko C, Sailer C, Zisser G, Marques-Carvalho MJ, Pellegrino S, Wawiorka L, et al. (2019). Mechanism of completion of peptidyltransferase centre assembly in eukaryotes. Elife 8, e44904. [PubMed: 31115337]

Kater L, Thoms M, Barrio-Garcia C, Cheng J, Ismail S, Ahmed YL, Bange G, Kressler D, Berninghausen O, Sinning I, et al. (2017). Visualizing the assembly pathway of nucleolar pre-60S ribosomes. Cell 171, 1599–1610 e14. [PubMed: 29245012]

Kater L, Mitterer V, Thoms M, Cheng J, Berninghausen O, Beckmann R, and Hurt E (2020). Construction of the central protuberance and L1 stalk during 60S subunit biogenesis. Mol. Cell 79, 615–628.e5. [PubMed: 32668200]

Khoshnevis S, Askenasy I, Johnson MC, Dattolo MD, Young-Erdos CL, Stroupe ME, and Karbstein K (2016). The DEAD-box protein Rok1 orchestrates 40S and 60S ribosome assembly by promoting the release of Rrp5 from pre-40S ribosomes to allow for 60S maturation. PLoS Biol. 14, e1002480. [PubMed: 27280440]

Klinge S, and Woolford JL JR. (2019). Ribosome assembly coming into focus. Nat. Rev. Mol. Cell Biol 20, 116–131. [PubMed: 30467428]

Konikkat S, and Woolford JL JR. (2017). Principles of 60S ribosomal subunit assembly emerging from recent studies in yeast. Biochem. J 474, 195–214. [PubMed: 28062837]

Kornprobst M, Turk M, Kellner N, Cheng J, Flemming D, Kos-Braun I, Kos M, Thoms M, Berninghausen O, Beckmann R, and Hurt E (2016). Architecture of the 90S pre-ribosome: a structural view on the birth of the eukaryotic ribosome. Cell 166, 380–393. [PubMed: 27419870]

Author Manuscript Author Manuscript Author Manuscript Author Manuscript

Kos-Braun IC, Jung I, and Koš M (2017). Tor1 and CK2 kinases control a switch between alternative ribosome biogenesis pathways in a growth-dependent manner. PLoS Biol. 15, e2000245. [PubMed: 28282370]

Kressler D, Hurt E, and Bassler J (2010). Driving ribosome assembly. Biochim. Biophys. Acta 1803, 673–683. [PubMed: 19879902]

Kressler D, Hurt E, and Bassler J (2017). A puzzle of life: crafting ribosomal subunits. Trends Biochem. Sci 42, 640–654. [PubMed: 28579196]

Krogan NJ, Peng WT, Cagney G, Robinson MD, Haw R, Zhong G, Guo X, Zhang X, Canadien V, Richards DP, et al. (2004). High-definition macromolecular composition of yeast RNA-processing complexes. Mol. Cell 13, 225–239. [PubMed: 14759368]

Leitner A, Walzthoeni T, and Aebersold R (2014). Lysine-specific chemical cross-linking of protein complexes and identification of cross-linking sites using LC-MS/MS and the xQuest/xProphet software pipeline. Nat. Protoc 9, 120–137. [PubMed: 24356771]

Liang X, Zuo MQ, Zhang Y, Li N, Ma C, Dong MQ, and Gao N (2020). Structural snapshots of human pre-60S ribosomal particles before and after nuclear export. Nat. Commun 11, 3542. [PubMed: 32669547]

Liu F, Rijkers DTS, Post H, and Heck AJR (2015). Proteome-wide profiling of protein assemblies by cross-linking mass spectrometry. Nat. Methods 12, 1179. [PubMed: 26414014]

Manikas RG, Thomson E, Thoms M, and Hurt E (2016). The K^+-dependent GTPase Nug1 is implicated in the association of the helicase Dbp10 to the immature peptidyl transferase centre during ribosome maturation. Nucleic Acids Res. 44, 1800–1812. [PubMed: 26823502]

Martin R, Straub AU, Doebele C, and Bohnsack MT (2013). DExD/H-box RNA helicases in ribosome biogenesis. RNA Biol. 10, 4–18. [PubMed: 22922795]

Milkereit P, Gadal O, Podtelejnikov A, Trumtel S, Gas N, Petfalski E, Tollervey D, Mann M, Hurt E, and Tschochner H (2001). Maturation and intranuclear transport of pre-ribosomes requires Noc proteins. Cell 105, 499–509. [PubMed: 11371346]

Oeffinger M, Zenklusen D, Ferguson A, Wei KE, El Hage A, Tollervey D, Chait BT, Singer RH, and Rout MP (2009). Rrp17p is a eukaryotic exonuclease required for 5' end processing of Pre-60S ribosomal RNA. Mol. Cell 36, 768–781. [PubMed: 20005841]

Ottoz DS, Rudolf F, and Stelling J (2014). Inducible, tightly regulated and growth condition-independent transcription factor in Saccharomyces cerevisiae. Nucleic Acids Res. 42, e130. [PubMed: 25034689]

Perez-Riverol Y, Csordas A, Bai J, Bernal-Llinares M, Hewapathirana S, Kundu DJ, Inuganti A, Griss J, Mayer G, Eisenacher M, et al. (2019). The PRIDE database and related tools and resources in 2019: improving support for quantification data. Nucleic Acids Res. 47, D442–D450. [PubMed: 30395289]

Pilion MC, Hsu AL, Krahn JM, Williams JG, Goslen KH, Sobhany M, Borgnia MJ, and Stanley RE (2019). Cryo-EM reveals active site coordination within a multienzyme pre-rRNA processing complex. Nat. Struct. Mol. Biol 26, 830. [PubMed: 31488907]

Rodríguez-Galán O, García-Gómez JJ, and de la Cruz J (2013). Yeast and human RNA helicases involved in ribosome biogenesis: current status and perspectives. Biochim. Biophys. Acta 1829, 775–790. [PubMed: 23357782]

Rosado IV, Dez C, Lebaron S, Caizergues-Ferrer M, Henry Y, and de la Cruz J (2007). Characterization of Saccharomyces cerevisiae Npa2p (Urb2p) reveals a low-molecular-mass complex containing Dbp6p, Npa1p (Urb1p), Nop8p, and Rsa3p involved in early steps of 60S ribosomal subunit biogenesis. Mol. Cell. Biol 27, 1207–1221. [PubMed: 17145778]

Rössler I, Embacher J, Pillet B, Murat G, Liesinger L, Hafner J, Unterluggauer JJ, Birner-Gruenberger R, Kressler D, and Pertschy B (2019). Tsr4 and Nap1, two novel members of the ribosomal protein chaperOME. Nucleic Acids Res. 47, 6984–7002. [PubMed: 31062022]

Röther S, Burkert C, Brünger KM, Mayer A, Kieser A, and Strässer K (2010). Nucleocytoplasmic shuttling of the La motif-containing protein Sro9 might link its nuclear and cytoplasmic functions. RNA 16, 1393–1401. [PubMed: 20494970]

Rudra D, Mallick J, Zhao Y, and Warner JR (2007). Potential interface between ribosomal protein production and pre-rRNA processing. Mol. Cell. Biol 27, 4815–4824. [PubMed: 17452446]

Author Manuscript Author Manuscript Author Manuscript Author Manuscript

Rusin SF, Adamo ME, and Kettenbach AN (2017). Identification of candidate casein kinase 2 substrates in mitosis by quantitative phosphoproteomics. Front. Cell Dev. Biol 5, 97. [PubMed: 29214152]

Sachs AB, and Davis RW (1990). Translation initiation and ribosomal biogenesis: involvement of a putative rRNA helicase and RPL46. Science 247, 1077–1079. [PubMed: 2408148]

Sanghai ZA, Miller L, Molloy KR, Barandun J, Hunziker M, Chaker-Margot M, Wang J, Chait BT, and Klinge S (2018). Modular assembly of the nucleolar pre-60S ribosomal subunit. Nature 556, 126–129. [PubMed: 29512650]

Schneider CA, Rasband WS, and Eliceiri KW (2012). NIH Image to ImageJ: 25 years of image analysis. Nat. Methods 9, 671–675. [PubMed: 22930834]

Schuller JM, Falk S, Fromm L, Hurt E, and Conti E (2018). Structure of the nuclear exosome captured on a maturing preribosome. Science 360, 219–222. [PubMed: 29519915]

Sharma S, Watzinger P, Kotter P, and Entian KD (2013). Identification of a novel methyltransferase, Bmt2, responsible for the N-1-methyl-adenosine base modification of 25S rRNA in Saccharomyces cerevisiae. Nucleic Acids Res. 41, 5428–5443. [PubMed: 23558746]

Taylor RG, Walker DC, and McInnes RR (1993). E. coli host strains significantly affect the quality of small scale plasmid DNA preparations used for sequencing. Nucleic Acids Res. 21, 1677–1678. [PubMed: 8479929]

Tyanova S, Temu T, and Cox J (2016a). The MaxQuant computational platform for mass spectrometry-based shotgun proteomics. Nat. Protoc 11, 2301–2319. [PubMed: 27809316]

Tyanova S, Temu T, Sinitcyn P, Carlson A, Hein MY, Geiger T, Mann M, and Cox J (2016b). The Perseus computational platform for comprehensive analysis of (prote)omics data. Nat. Methods 13, 731–740. [PubMed: 27348712]

van den Berg S, Löfdahl P-A, Härd T, and Berglund H (2006). Improved solubility of TEV protease by directed evolution. J. Biotechnol 121, 291–298. [PubMed: 16150509]

Wade CH, Umbarger MA, and McAlear MA (2006). The budding yeast rRNA and ribosome biosynthesis (RRB) regulon contains over 200 genes. Yeast 23, 293–306. [PubMed: 16544271]

Walzthoeni T, Claassen M, Leitner A, Herzog F, Bohn S, Forster F, Beck M, and Aebersold R (2012). False discovery rate estimation for cross-linked peptides identified by mass spectrometry. Nat. Methods 9, 901–903. [PubMed: 22772729]

Woolford JL JR., and Baserga SJ (2013). Ribosome biogenesis in the yeast Saccharomyces cerevisiae. Genetics 195, 643–681. [PubMed: 24190922]

Wu S, Tutuncuoglu B, Yan K, Brown H, Zhang Y, Tan D, Gamalinda M, Yuan Y, Li Z, Jakovljevic J, et al. (2016). Diverse roles of assembly factors revealed by structures of late nuclear pre-60S ribosomes. Nature 534, 133–137. [PubMed: 27251291]

Yang J, Sharma S, Watzinger P, Hartmann JD, Kötter P, and Entian KD (2016). Mapping of complete set of ribose and base modifications of yeast rRNA by RP-HPLC and mung bean nuclease assay. PLoS One 11, e0168873. [PubMed: 28033325]

Yao Y, Demoinet E, Saveanu C, Lenormand P, Jacquier A, and Fromont-Racine M (2010). Ecm1 is a new pre-ribosomal factor involved in pre-60S particle export. RNA 16, 1007–1017. [PubMed: 20348449]

Yoo CJ, and Wolin SL (1997). The yeast La protein is required for the 3' endonucleolytic cleavage that matures tRNA precursors. Cell 89, 393–402. [PubMed: 9150139]

Zhou D, Zhu X, Zheng S, Tan D, Dong MQ, and Ye K (2019a). Cryo-EM structure of an early precursor of large ribosomal subunit reveals a half-assembled intermediate. Protein Cell 10, 120–130. [PubMed: 29557065]

Zhou Y, Musalgaonkar S, Johnson AW, and Taylor DW (2019b). Tightly-orchestrated rearrangements govern catalytic center assembly of the ribosome. Nat. Commun 10, 958. [PubMed: 30814529]

Author Manuscript Author Manuscript Author Manuscript Author Manuscript

Highlights

- Comprehensive resource of 60S ribosome biogenesis factors in the yeast *S. cerevisiae*
- Time-resolved interaction map of RBF engagement during 60S maturation
- Localization of 22 previously unmapped RBFs to specific biogenesis intermediates
- Interaction map and timing of 60S engagement by the DEAD-box ATPases Dbp9 and Dbp10

Author Manuscript Author Manuscript Author Manuscript Author Manuscript

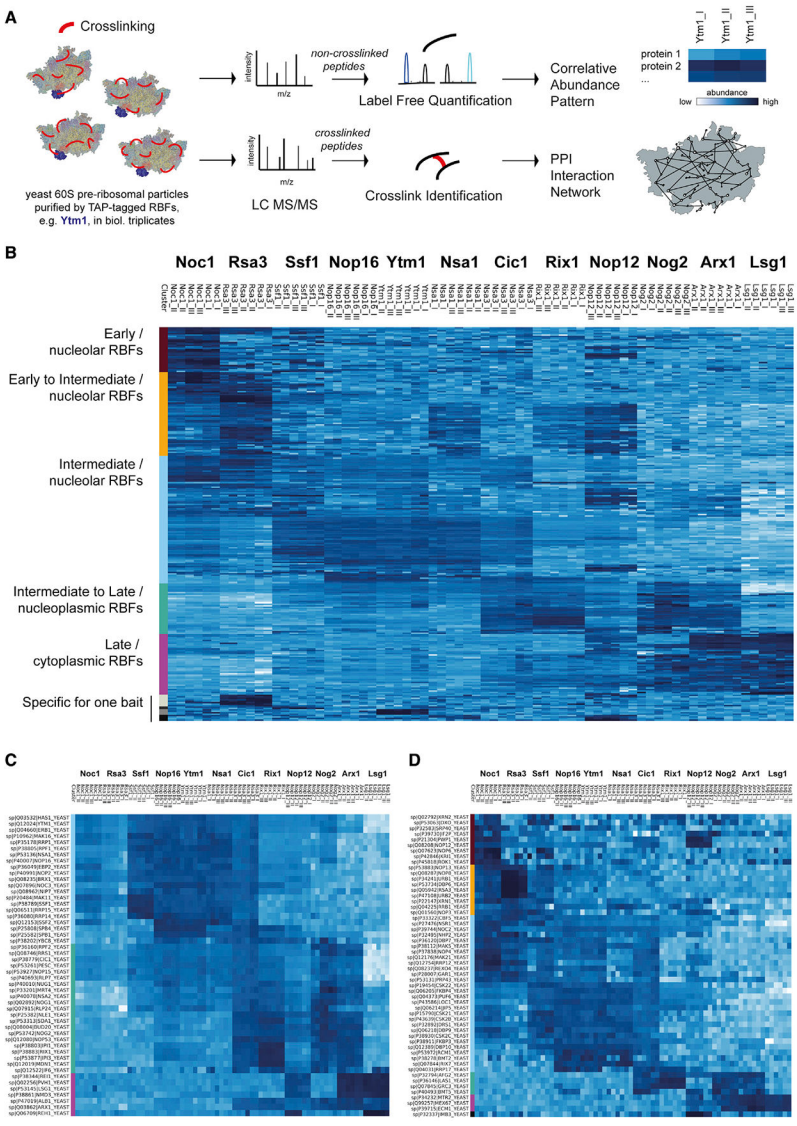

Figure 1. Timeline of 60S ribosomal biogenesis

(A) Schematic overview of our AP-MS LFQ and XL-MS workflow. Different RBFs were used to affinity purify 60S pre-ribosomal particles. Particles were crosslinked and analyzed by liquid chromatography-tandem mass spectrometry (LC-MS/MS). Non-crosslinked peptides were used for the identification and quantification of proteins, and crosslinked peptides were used to obtain particle-specific PPIs.

(B) Heatmap of all 272 proteins, which were reliably identified and quantified in pre-ribosomal particles from 12 different RBFs used as bait proteins (biological triplicates; n = 3). RBFs used as bait proteins (x axis) are shown at top and are plotted versus their respective interactors (y axis). Protein abundances are sorted by unbiased hierarchical clustering and are shown from early to late assembly states (see STAR Methods for details).

(C) Abundance pattern of RBFs with known localization from previous pre-60S high-resolution studies.

Author Manuscript Author Manuscript Author Manuscript Author Manuscript

(D) Abundance pattern of RBFs for which no structural information at pre-ribosomal particles has been available so far.

Author Manuscript Author Manuscript Author Manuscript Author Manuscript

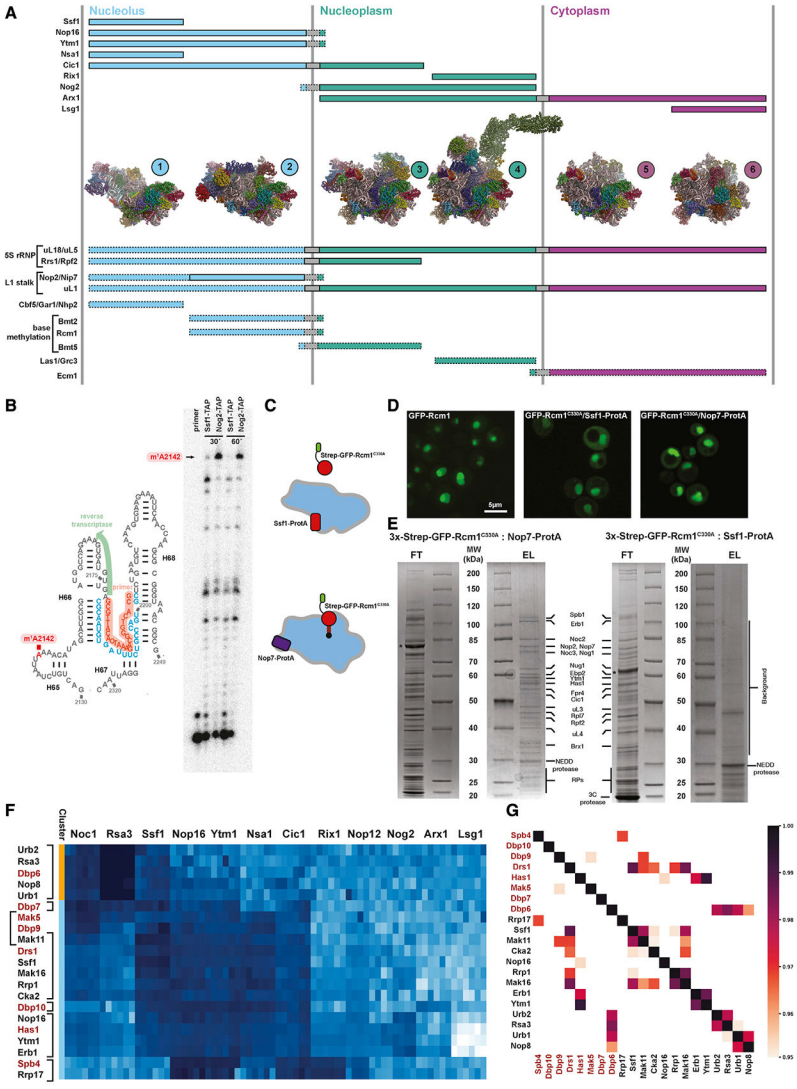

Figure 2. Assigning structurally uncharacterized RBFs to specific 60S cryo-EM reconstructions

(A) Top: Distribution of affinity-tagged RBFs used for our timeline among representative models derived from pre-60S cryo-EM reconstructions. Center: Nucleolar pre-60S intermediates: 1 (PDB: 6EM1), 2 (PDB: 6ELZ); nucleoplasmic pre-60S intermediates: 3 (PDB: 3JCT), 4 (PDB: 6YLH); cytoplasmic pre-60S intermediates: 5 (PDB: 6N8J), and 6 (PDB: 6RZZ). Bottom: Extended distribution of 5S rRNP (uL5, uL18, Rpf2, and Rrs1) and L1 stalk (Nop2, Nip7, and uL1) complexes to early nucleolar intermediates based on quantitative MS data (dashed boxes) and association of rRNA-modifying enzymes to distinct pre-60S structural intermediates derived from correlation with quantitative MS data. Color patterns are the same as in Figure 1.

(B) Schematic of 25S rRNA showing DNA primer sites at positions 2,178–2,201 and methylation site at m^1A2142 (left). A primer extension assay (right) shows the different cDNA fragments on pre-25S rRNA of purified Ssf1-tagged and Nog2-tagged intermediates, with a distinct band corresponding to m^1A2142 in the nucleoplasmic Nog2 particles.

(C) Schematic of Rcm1 trapping strategy.

Author Manuscript Author Manuscript Author Manuscript Author Manuscript

(D) Fluorescent live cell images of overexpressed GFP-tagged Rcm1 (left) and Rcm1^{C330A} with an Ssf1 (center) or Nop7 (right) secondary tag show that crosslinked Rcm1 is diffusely distributed in the cells compared to the wild-type protein.

(E) Coomassie gels of StrepTrap column flowthrough (FT) or elution (EL) for the Rcm1^{C330A} following the initial selection of Nop7- (left) or Ssf1- (right)containing particles on IgG columns. The positions of key late nucleolar proteins are indicated by arrows in the Nop7 elution lane and the Ssf1 flowthrough lane.

(F) Heatmap of abundance patterns of DEAD-box ATPases in our timeline, along with most closely associated factors as determined by Pearson correlations. Close associations of DEAD-box proteins (highlighted in red) are bracketed.

(G) Heatmap of pairwise Pearson correlations of the proteins shown in (F) DEAD-box proteins are labeled in red. Correlations ≥0.95 are shown and colored according to the legend.

Author Manuscript Author Manuscript Author Manuscript Author Manuscript

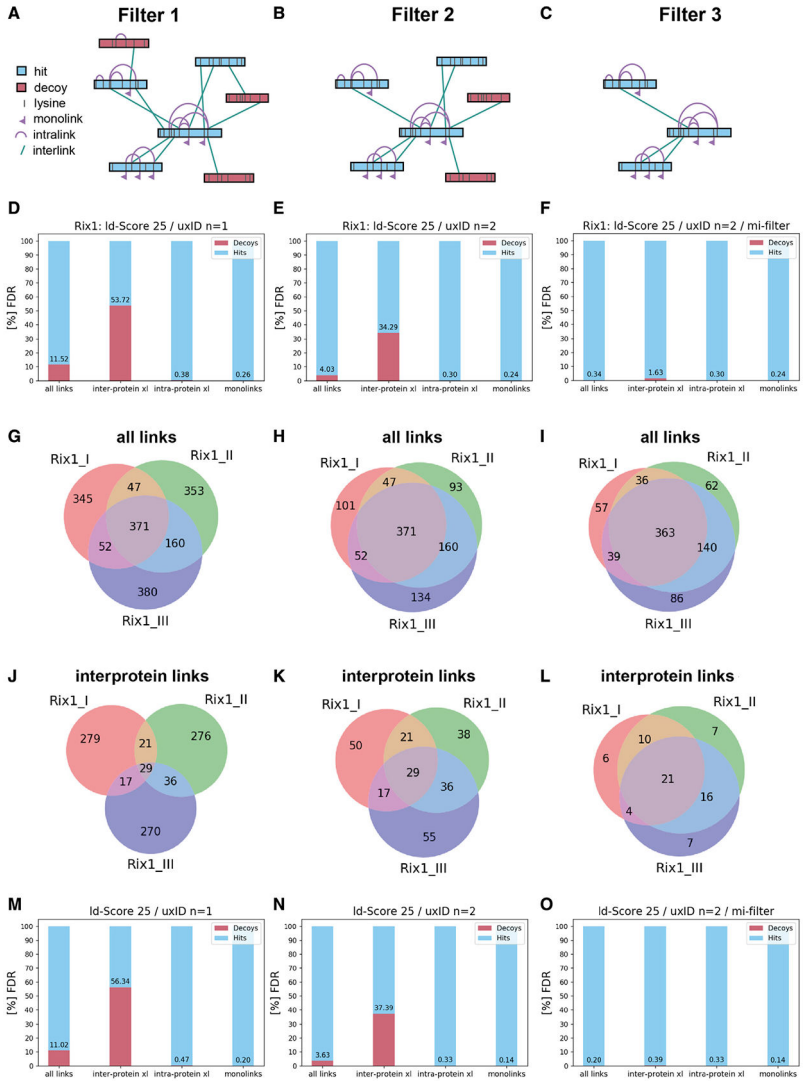

Figure 3. Mono- and intralink filter (mi-filter) for XL-MS data

Illustration of different filter criteria and their influence on the FDRs in our crosslink dataset. Shown are true-positive crosslinks (hits) in blue and false-positive (decoys) in red.

(A) The “standard” filter setting relies on 1 identified high-confidence crosslink per unique crosslinking site.

(B) The more stringent filter setting relies on 2 independently identified high-confidence crosslinks per unique crosslinking site (among all datasets).

(C) For the final filter setting, the mi-filter was applied (n = 3).

(D–F) Bar charts for each filter setting and the respective FDRs (shown in percentages) for all link types for the Rix1 dataset.

(G–L) Venn diagrams showing the overlap between the three independent biological replicates (n = 3) of the Rix1 particle for all link-types (G–I) and (J–L) for interprotein crosslinks only.

(M–O) Bar charts for each filter setting and the respective FDRs (shown in percentages) for all link types in our whole dataset. For H, I, K, and L, all of the links, which were identified

Author Manuscript Author Manuscript Author Manuscript Author Manuscript

in only 1 biological replicate of Rix1 pre-ribosomal particles, were also identified in at least 1 other pre-ribosomal particle.

Author Manuscript Author Manuscript Author Manuscript Author Manuscript

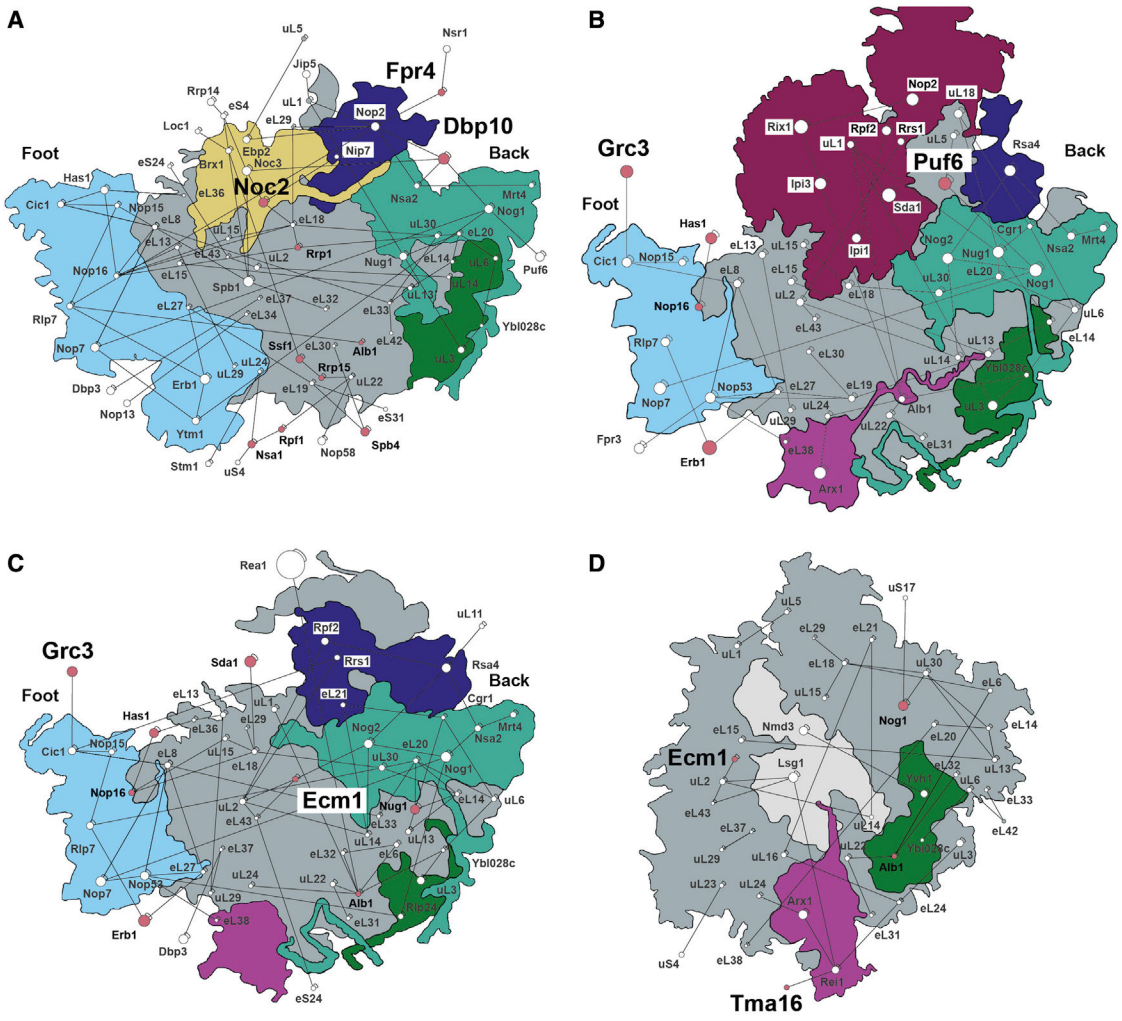

Figure 4. High-confidence crosslink networks

Shown are high-confidence crosslinks using our mi-filter for a select subset of RBFs from our AP-MS XL-MS dataset mapped onto corresponding previously published cryo-EM reconstructions.

(A) Crosslinks of the Ytm1 pre-ribosomal particle mapped onto PDB: 6ELZ.

(B) Crosslinks of the Rix1 pre-ribosomal particle mapped onto PDB: 6YLH.

(C) Crosslinks of the Nog2 pre-ribosomal particle mapped onto PDB: 3JCT.

(D) Crosslinks of the Lsg1 pre-ribosomal particle mapped onto PDB: 6RZZ. RBFs that were identified within a particle-specific crosslinking dataset (n = 2) but are not present in the respective PDB structure (although present in some other PDB structures) are indicated in red and labeled in boldface, while RBFs and factors with presently unknown positions (Noc2, Fpr4, Dbp10, Grc3, Puf6, Ecm1, and Tma16) are labeled with a larger font size. For a description of the highlighted regions, see Figure S6. Proteins containing only intra- or monolinks are not shown.

Author Manuscript Author Manuscript Author Manuscript Author Manuscript

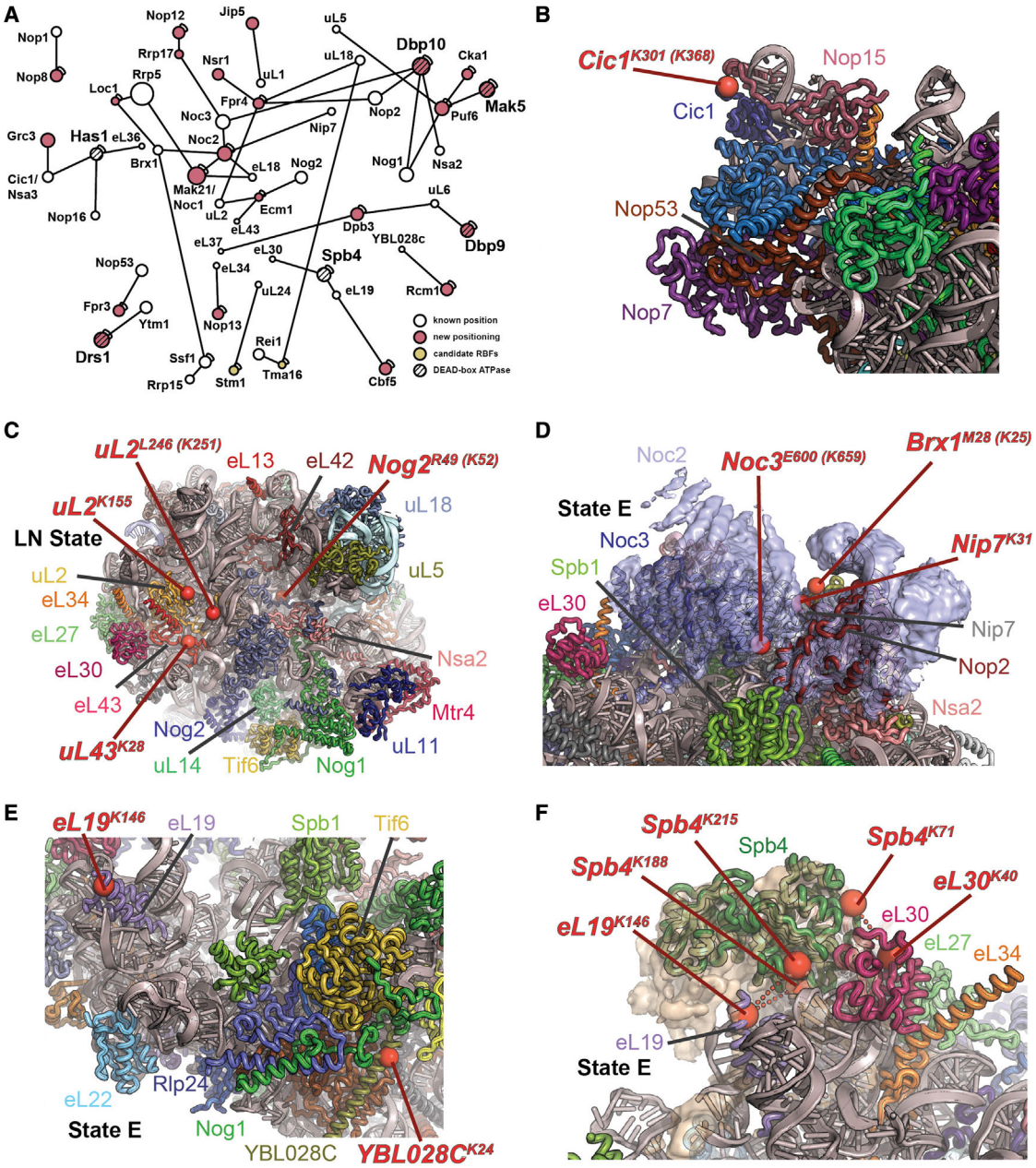

Figure 5. Placement of structurally uncharacterized RBFs

(A) Map of mi-filtered high-confidence crosslinks from our complete AP-MS XL-MS dataset for candidate biogenesis factors and all RBFs whose localization within pre-ribosomal particles are not known. New localizations for known RBFs are shown in red and for additional RBFs with a potential role in 60S biogenesis are shown in yellow. DEAD-box ATPases additionally contain black stripes.

(B) Illustration of the foot structure in the nucleoplasmic Nog2 particle (PDB: 3JCT) (Wu et al., 2016). The closest modeled residue K301 to the position of the Cic1-Grc3 crosslink (K363) (Cic1$^{K301(K363)}$) is shown as a red sphere.

Author Manuscript Author Manuscript Author Manuscript Author Manuscript

(C) Placement of Ecm1 on nucleoplasmic pre-60S particles. Illustration of PDB:6N8J (Zhou et al., 2019b), with key proteins labeled. Residues with interlinks (or closest modeled residue if disordered) to Ecm1 are shown as red spheres and labeled. The only access to residue K52 of Nog2 is in the post-rotation state before Nmd3 binding.
(D) Assignment of Noc2 to uncharacterized EM density in late nucleolar 60S particles. Illustration of PDB: 6ELZ with overlaid EM density (EMDB: 3891) (Kater et al., 2017), low pass filte red to 4Å. Key proteins are labeled. Red spheres mark the position of residues (or closest modeled residue, if disordered) of Noc3, Brx1, or Nip7 that form interprotein crosslinks to Noc2. The features of the density are consistent with the prediction that Noc2 forms helical repeats and directly interacts with Noc3.
(E) Positions of crosslinks to Cbf5 (eL19^{K146}) and Rcm1 (YBL028C^{K24}) mapped as red spheres onto the State E molecular model (PDB: 6ELZ) (Kater et al., 2017).
(F) Docked homology model of Spb4 into the extra density of State E (EMDB: 3891) (Kater et al., 2017) and positions of crosslinks between Spb4 and eL19 and Spb4 and eL30 (red spheres and dashed lines).

Author Manuscript Author Manuscript Author Manuscript Author Manuscript

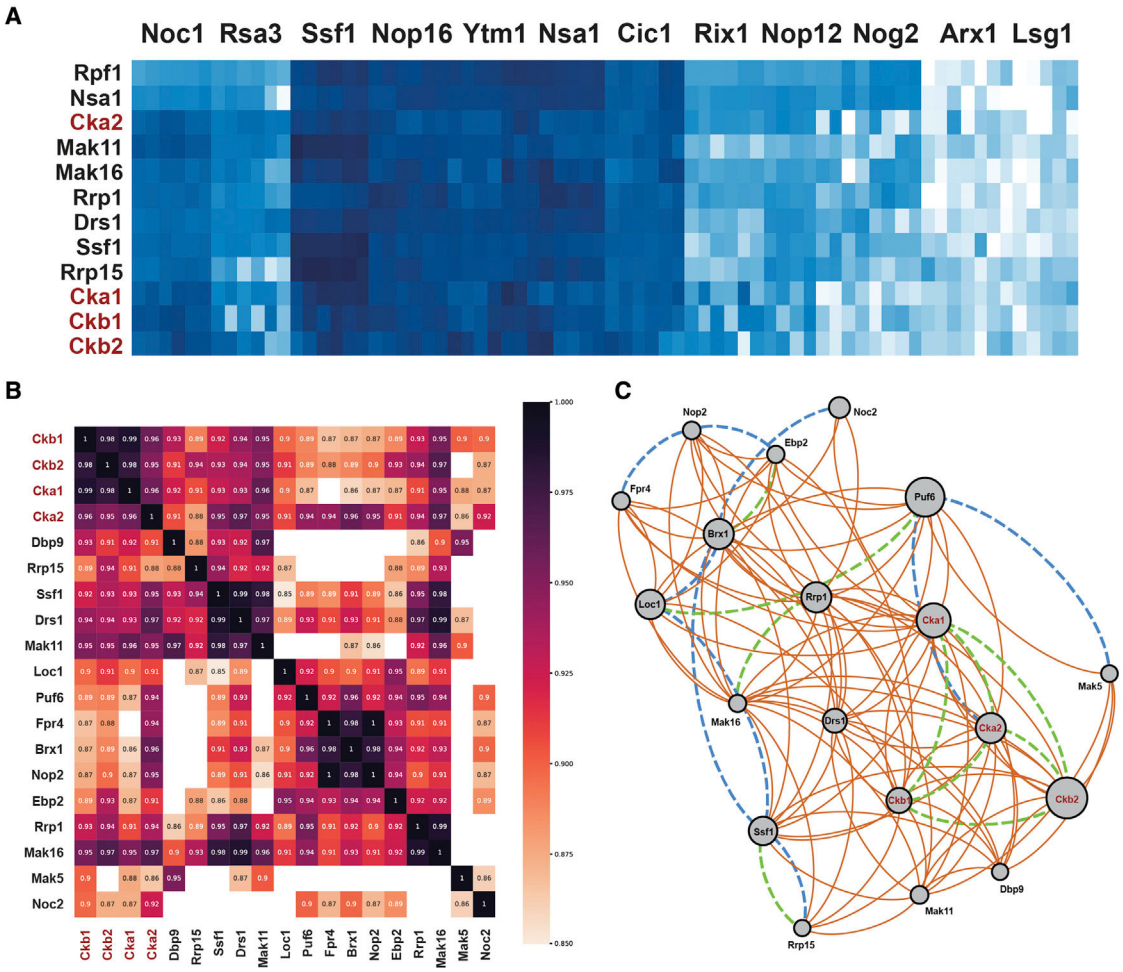

Figure 6. The casein kinase complex is a 60S biogenesis factor

(A) Protein abundance subcluster for the Ck2 complex (n = 3).

(B) Heatmap of pairwise correlations within the Ck2 interactome.

(C) The Ck2 interactome during 60S biogenesis. Shown are direct physical interactions identified by high-confidence interlinks (blue dotted lines) or known structural interactions (green dotted lines), as well as indirect interactions identified by correlations of protein abundance in different 60S intermediate particles indicating a temporal coordination (solid orange lines, see B).

Author Manuscript Author Manuscript Author Manuscript Author Manuscript

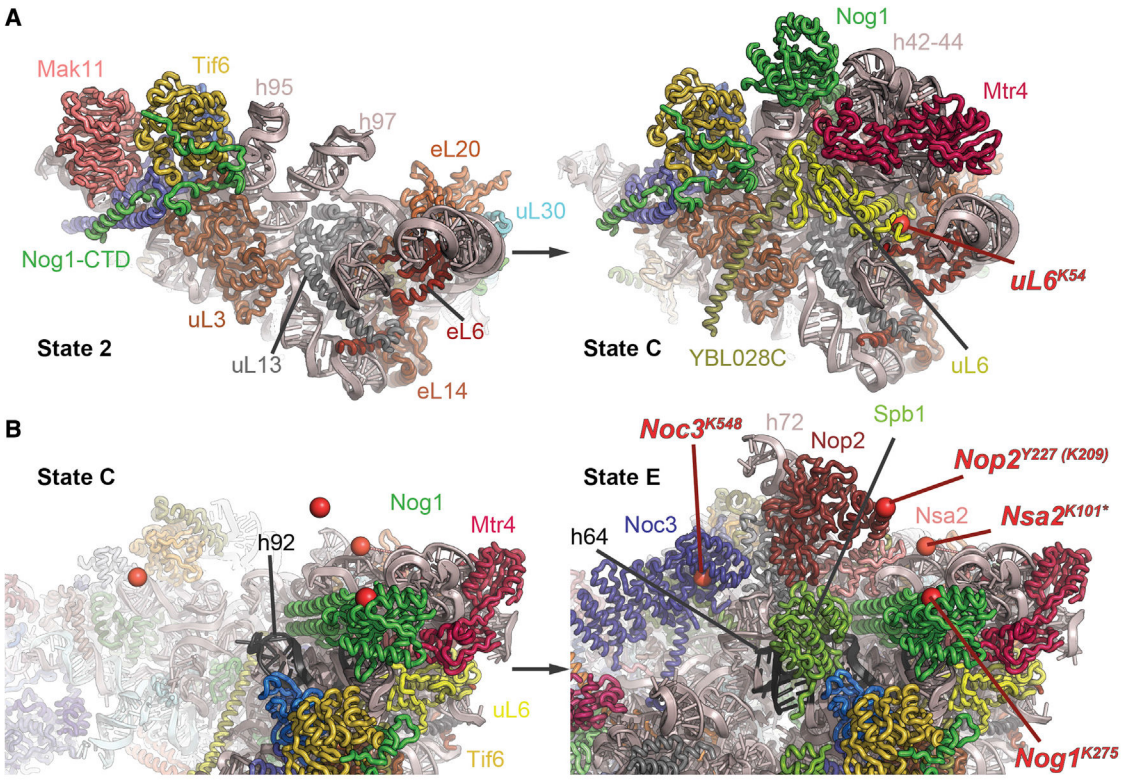

Figure 7. Placement of DEAD-box ATPases Dbp9 and Dbp10

(A) Illustration of early nucleolar pre-60S particles (left, PDB: 6C0F; right, PDB: 6EM1), showing the final assembly of RBFs engaging rRNA domain VI. The transition is defined by the release of Mak11 and the binding of uL6, Nsa2, and Mrt4, as well as the N-terminal GTPase domain of Nog1. The N-terminal RecA domain of Dbp9 crosslinks to uL6, indicating that it engages 60S during the final assembly of this region of the 60S ribosome. (B) Dbp10 engages the pre-60S ribosome after the Noc3 binding, but before engagement of helix 92 by the methyltransferase domain of Spb1. Left: Illustration of nucleolar pre-60S intermediate (PDB: 6EM1) with key proteins labeled. Residues with specific crosslinks to Dbp10 are shown as red spheres, revealing that the majority of interacting residues are not yet ordered. Right: Crosslinked residues are present in the late nucleolar 60S structure (PDB: 6ELZ), but the likely interaction site with rRNA on helices h64 and h92 is occupied by the methyltransferase domain of Spb1, suggesting that Dbp10 engages the pre-60S before Spb1 catalysis.

Author Manuscript Author Manuscript Author Manuscript Author Manuscript

KEY RESOURCES TABLE

REAGENT or RESOURCE	SOURCE	IDENTIFIER
Bacterial and virus strains		
E. coli DH5α	Taylor et al., 1993	N/A
Chemicals, peptides, and recombinant proteins		
Bacto™ Peptone	Gibco™ (ThermoFisher Scientific)	Cat#211820
Bacto™ Yeast Extract	Gibco™ (ThermoFisher Scientific)	Cat#212720
IgG Sepharose™ 6 Fast Flow	Cytiva (formerly GE Healthcare)	Cat#17-0-0969-01
Calmodulin Affinity Resin	Agilent Technologies	Cat#214303
DSS-H12/D12 (disuccinimidyl suberate)	Creative Molecules Inc.	Cat#001S
Sequencing grade trypsin	Promega	Cat#V5113
^{32}P-ATP	Hartmann Analytic	Cat#FP-401
T4 polynucleotide kinase	New England BioLabs	Cat#M0201S
Sephadex-G25 superfine	Cytiva (formerly GE Healthcare)	Cat#17003101
Invitrogen™ SuperScript™ III reverse transcriptase	Fisher Scientific	Cat#10432122
Critical commercial assays		
RNA Clean & Concentrator 25 Kit	Zymo Research	Cat#R1018
Deposited data		
The MS raw files, MaxQuant search parameters as well as the 'combined' results folder of MaxQuant, the crosslink database and original *xQuest* result files and final mi-filtered crosslink data have all been deposited to the ProteomeXchange Consortium via the PRIDE partner repository.	PRIDE; Perez-Riverol et al., 2019	Project accession number PXD021831
Experimental models: Organisms/strains		
S. cerevisiae: BY4741 strain: TAP-tagged Mak21/Noc1 (YDR060W)	Dharmacon™ Horizon Discovery	Cat#YSC1178-202230367
S. cerevisiae: BY4741 strain: TAP-tagged Rsa3 (YLR221C)	Dharmacon™ Horizon Discovery	Cat#YSC1178-202232410
S. cerevisiae: BY4741 strain: TAP-tagged Ssf1 (YHR066W)	Dharmacon™ Horizon Discovery	Cat#YSC1178-202231472
S. cerevisiae: BY4741 strain: TAP-tagged Nop16 (YER002W)	Dharmacon™ Horizon Discovery	Cat#YSC1178-202230774
S. cerevisiae: BY4741 strain: TAP-tagged Ytm1 (YOR272W)	Ghaemmaghami et al., 2003	N/A
S. cerevisiae: BY4741 strain: TAP-tagged Nsa1 (YGL111W)	Dharmacon™ Horizon Discovery	Cat#YSC1178-202231086
S. cerevisiae: BY4741 strain: TAP-tagged Cic1/Nsa3 (YHR052W)	Dharmacon™ Horizon Discovery	Cat#YSC1178-202231461
S. cerevisiae: BY4741 strain: TAP-tagged Rix1 (YHR197W)	Ghaemmaghami et al., 2003	N/A
S. cerevisiae: BY4741 strain: TAP-tagged Nop12 (YOL041C)	Dharmacon™ Horizon Discovery	Cat#YSC1178-202233257
S. cerevisiae: BY4741 strain: TAP-tagged Nog2 (YNR053C)	Ghaemmaghami et al., 2003	N/A
S. cerevisiae: BY4741 strain: TAP-tagged Arx1 (YDR101C)	Ghaemmaghami et al., 2003	N/A
S. cerevisiae: BY4741 strain: TAP-tagged Lsg1 (YGL099W)	Ghaemmaghami et al., 2003	N/A

Author Manuscript Author Manuscript Author Manuscript Author Manuscript

REAGENT or RESOURCE	SOURCE	IDENTIFIER
S. cerevisiae: BY4741 strain: TAP-tagged Cka1 (YIL035C)	Dharmacon™ Horizon Discovery	Cat#YSC1178-202231607
S. cerevisiae: BY4741: his3-1, leu2-0, met15-0, ura3-0	Brachmann et al., 1998	N/A
S. cerevisiae: RCM1: BY4741, $P_{minCYC1}$-sfGFP-2xStrep-bdNEDD8-MYC-*RCM1*::URA3	This manuscript	N/A
S. cerevisiae: RCM1: BY4741, $P_{minCYC1}$-sfGFP-2xStrep-bdNEDD8-MYC-*rcm1*^{C330A}::URA3, NOP7-FLAG-3C-ProtA::HygR	This manuscript	N/A
S. cerevisiae: RCM1: BY4741, $P_{minCYC1}$-sfGFP-2xStrep-bdNEDD8-MYC-rcm1^{C330A}::URA3, SSF1-FLAG-3C-ProtA::HygR	This manuscript	N/A
S. cerevisiae: BY4741, TMA16-FLAG-3C-ProtA::HygR	This manuscript	N/A
Oligonucleotides		
DNA primer, see Figure 2B: complementary to 25S rRNA nt 2178-2202: GCACTGGGCAGAAATCACATTGCG	Sharma et al. (2013)	N/A
Recombinant DNA		
pRS406-custom pLEXA-minCYC1 sfGFP-3xStrep-bdNEDD8-MYC-*RCM1*-CYC1t	This manuscript	N/A
pRS406-custom pLEXA-minCYC1 sfGFP-3xStrep-bdNEDD8-MYC-*rcm1*^{C330A}-CYC1t	This manuscript	N/A
Plasmid pTH24 TEV	van den Berg et al., 2006	N/A
Software and algorithms		
MaxQuant 1.6.5.0	Tyanova et al. (2016a)	https://www.maxquant.org/
Perseus 1.6.5.0	Tyanova et al. (2016b)	https://www.maxquant.org/perseus/
xQuest 2.1.3	Leitner et al. (2014)	http://proteomics.ethz.ch/cgi-bin/xquest2_cgi/download.cgi
xProphet 2.1.3	Leitner et al. (2014)	http://proteomics.ethz.ch/cgi-bin/xquest2_cgi/download.cgi
xiNET	Combe et al. (2015)	http://crosslinkviewer.org/
ImageJ	Collins (2007), Schneider et al., 2012	https://imagej.nih.gov/ij/
Other		
Swinging mill MM 400	Retsch®	Cat#20.745.0001
Amicon Ultracel-10, 0.5 mL	Merck Millipore	Cat#UFC501096
Amicon Ultracel-100, 0.5 mL	Merck Millipore	Cat#UFC510096
Sep-Pak tC18 Cartridge	Waters	Cat#WAT054960
Poly-Prep® chromatography columns	BioRad	Cat#731-1550
äKTA™ pure micro system	Cytiva (formerly GE Healthcare)	Cat#29302479
Superdex 30 Increase 3.2/300	Cytiva (formerly GE Healthcare)	Cat#29219758
Orbitrap Fusion™ Tribrid™ mass spectrometer	ThermoFisher Scientific	Cat#IQLAAEGAAPFADBMBCX
EASY-nLC™ 1200 system	ThermoFisher Scientific	Cat#LC140
Acclaim™ PepMap™ RSLC	ThermoFisher Scientific	Cat#164943
TGradient Thermoblock	Biometra	Cat#050-801
Typhoon™ FLA 9500	Cytiva (formerly GE Healthcare)	Cat#29-0040-80

REAGENT or RESOURCE	SOURCE	IDENTIFIER
Pulverisette 6 grinding ball mill	Fritsch	Cat#06.2000.00

Author Manuscript
Author Manuscript
Author Manuscript
Author Manuscript